VISTA Status Report
June 2007

H. Ceric, S. Dhar, G. Karlowatz,
L. Li, M. Pourfath, S. Selberherr

Institute for Microelectronics
Technical University Vienna
Gußhausstraße 27-29
A-1040 Wien, Austria

Contents

1 Intrinsic Stress Build-Up During Volmer-Weber Crystal Growth **1**

1.1 Introduction 1

1.2 Theoretical Considerations 1

1.3 Simulation Results and Discussion 1

1.4 Conclusion 3

2 High-Field Electron Mobility Model for Strained Si Devices **4**

2.1 Introduction 4

2.2 High-Field Electron Transport in Strained Silicon 4

2.3 Analytical High Field Velocity Model 6

2.3.1 Parallel Velocity Model 7

2.3.2 Perpendicular Velocity Model 7

2.3.3 Total Velocity for Fixed Field Direction 8

2.3.4 Total Velocity for Arbitrary Field Direction 8

2.4 Implementation Issues 10

2.5 Conclusion 10

3 Analysis of Hole Transport in Arbitrarily Strained Germanium **12**

3.1 Introduction 12

3.2 Band Structure Calculation 12

3.3 The Vienna Monte Carlo Simulator 12

3.4 Results 15

3.5 Conclusion 16

4 Carrier Concentration Dependence of the Mobility in Organic Semiconductors **17**

4.1 Introduction 17

4.2 Theory 17

4.3 Conclusion 19

5 Optimal Design for Carbon Nanotube Transistors **20**

5.1 Introduction 20

5.2 Approach 20

5.2.1 Static Response 20

5.2.2 Dynamic Response 21

5.3 Simulation Results 21

5.4 Conclusion 23

1 Intrinsic Stress Build-Up During Volmer-Weber Crystal Growth

We present a model for build-up of intrinsic stress during the deposition of thin metal films. The model assumes a three-phase stress generation mechanism which corresponds to three characteristic phases of microstructure evolution. The simulation results based on the model are successfully compared with experimental results for Poly-SiGe PECVD films. The impact of critical parameter variation on mechanical properties of thin film is discussed.

1.1 Introduction

Residual mechanical stress introduced during deposition of thin films and coatings has a significant impact on the reliability of electronic devices and structural components. The mechanical stress in thin metal films consists of a thermal component and an intrinsic component due to the evolution of the metal microstructure during film growth.

The goal of this work is the integration of the respective models for the specific phases of microstructural evolution into a comprehensive model which describes the intrinsic stress behavior during the entire deposition process. This model can be used to assess and optimize the mechanical stability of multilayer structures.

1.2 Theoretical Considerations

The model introduced here is based on the work presented in [1, 2, 3]. For the sake of generality we define our model in the sense of strain which is developed during the deposition of a metal film due to microstructural evolution. We combine three microstrain generation mechanisms, each arising in the characteristic phase of thin film growth (Fig. 1).

In the initial phase we assume the so-called Volmer-Weber growth which includes a build-up of a strong compressive stress component due to the Laplace pressure of isolated material islands [1]. It is followed by a tensile stress mechanism which operates during the island coalescence phase and thereafter [1]. The third phase introduces again a compressive component, but this time due to adatom insertion into the top of the grain boundaries (Fig. 2). The basic feature of our approach is an introduction of the strain-gradient function $\omega(z,r)$ which depends on the grain size distribution function $L(z)$ and material deposition rate r. $L(z)$ can be obtained by using several different algorithms which simulate the morphology evolution of the thin film microstructure according to the Van der Drift mechanism [4]. An example concerning the Van der Drift growth for a representative group of 9 grains is given in Fig. 3 and Fig. 4. The evolution of the microstrain $\varepsilon^I(z,r)$ in the direction of the film growth is given by (1). The microstrain consists of the contribution from the first phase $\varepsilon_{t,1}(z_i,r)$, where z_i is the film thickness after a coalescence, and an integral term relating to microstrain development in the second and the third phase (2),

$$\varepsilon^I(z,r) = \varepsilon_{t,1}(z_i,r) + \int_{z_i}^{z} \omega(w,r)\,dw, \qquad (1)$$

$$\omega(z,r) = \omega_{t,2}(z,r) + \omega_{c,3}(z,r). \qquad (2)$$

The strain-gradient function $\omega(z,r)$ consists of a tensile ($\omega_{t,2}(z,r)$) and a compressive ($\omega_{c,3}(z,r)$) component. The third phase compressive contribution $\omega_{c,3}(z,r)$ (3) depends on the jumping frequency Γ_c of adatoms into a grain boundary (Fig. 2) and adatom concentrations C_a, C_0, at the top of the grain boundary and elsewhere on the grain surface, respectively [1]. ε^* is the local strain at the top of the grain and $\beta = \Omega M/kT$ [1].

$$\omega_{c,3}(z,r) = -\frac{2\,\Omega\,\Gamma_c}{L(z)\,r}\Big(C_a - C_0\,e^{-\beta\varepsilon^*}\Big) \qquad (3)$$

The straightforward way to apply a microstrain model on larger multilayer structures is given by using linear elastic theory. In this case the microstrain acts as residual stress,

$$\sigma(x,y,z) = \mathbf{D}(\varepsilon(x,y,z) - \varepsilon^I(z,r)\mathbf{I}). \qquad (4)$$

The overall mechanical problem is defined by the equilibrium condition $\nabla\sigma = 0$. The obtained system of partial differential equations is solved by means of the finite element method.

1.3 Simulation Results and Discussion

Since our model is defined for general Volmer-Weber crystal growth, it can be applied for a multitude of different metals and deposition processes. For example, a well established fact is that AlN, copper, and SiGe thin films deposited on a Si/SiO_2 layer exhibit Volmer-Weber growth with three distinctive stress generation phases ([1, 5, 3]). We have applied our model for Poly-SiGe PECVD thin film deposition [6]. For an experimental thin film deflection a microstrain curve has been extracted in our previous work [7]. The comparison between this experimental microstrain and the microstrain obtained by the presented three-phase model is given in Fig. 5. Three phases of the microstructure are clearly

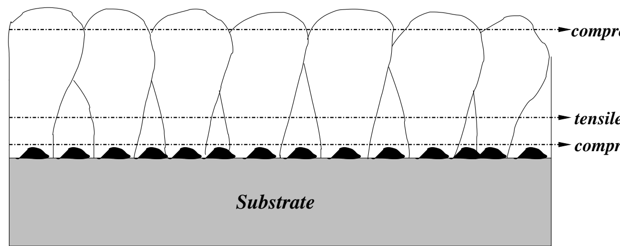

Figure 1: V-shape grain growth.

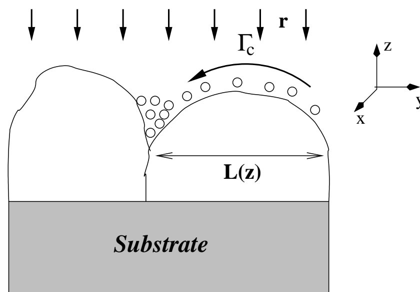

Figure 2: Third phase. Adatoms are inserted between the grain boundaries.

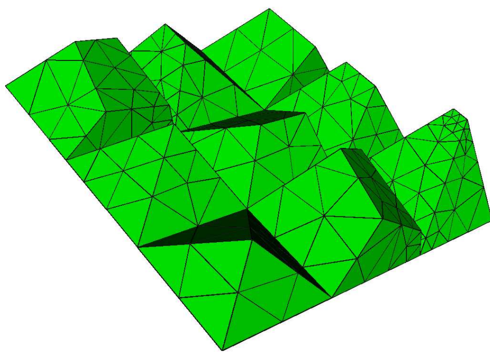

Figure 3: Grains after coalescence.

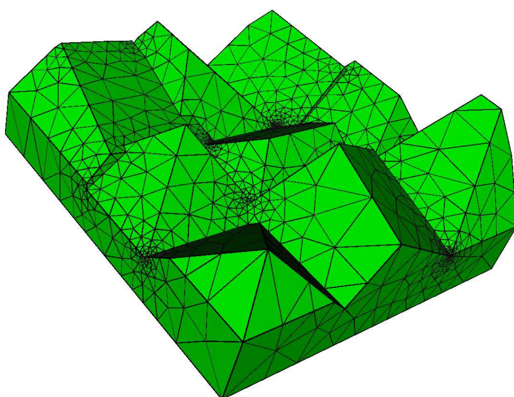

Figure 4: Grains after Van der Drift growth.

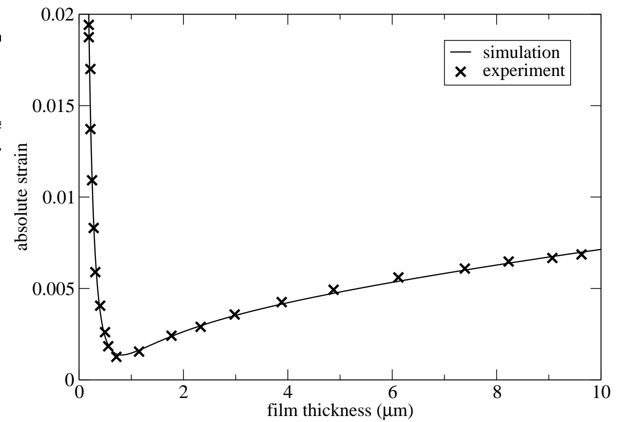

Figure 5: Comparison between experimentally determined microstrain with simulation.

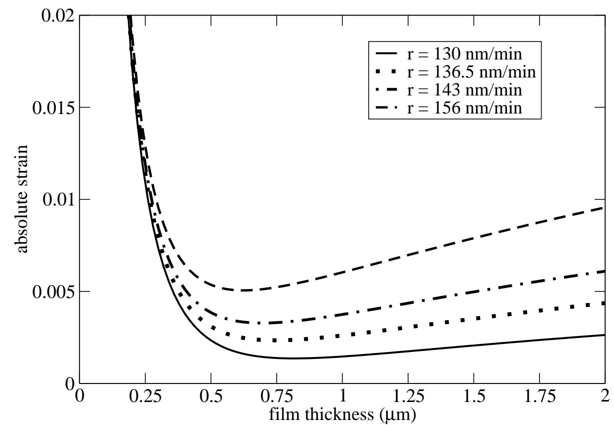

Figure 6: The effect of deposition rate variation.

recognizable in the microstrain curve. The resulting profile lays completely in the area of compressive strain, because the compressive contribution dominates over tensile one. In the first part of the microstrain curve (Fig. 5), a high compressive component from the first phase can be seen. The curve further sinks (but it remains positive) indicating an impact of the tensile component which bears a negative sign. Continued growth of V-shaped grains introduces a final compressive component of the third phase. Numerous experimental observations have shown that the variation of process conditions of SiGe PECVD after reaching the third phase [5] does not disrupt the growth of individual grains. Changing the deposition rate or germanium concentration can increase or reduce the number of adatoms arriving at the top of the grain boundary, the mobility of the adatoms can be influenced by changing process temperature and germanium concentration, but grains continue their growth [5]. However, measurements clearly show that the resulting strain in the film changes. The effect of the deposition

rate variation on microstrain is given in Fig. 6. From this picture we can conclude that increasing the deposition rate enhances the compressive component from the third phase of the growth process. Increasing of the deposition rate to 5 %, 10 %, and 20 %, causes an increase of the third phase compressive component to 65 %, 131 %, and 263 %, for 2 μm film thickness, respectively. This effect can be practically used for design of the so-called compensation layers at the final stage of thin film deposition for MEMS applications [5].

1.4 Conclusion

In this work we have presented a three phase model for evolution of microstrains in deposited thin metal films. Since our model considers a general dynamics of formation and evolution of grains, it can be applied to a wide spectrum of technological processes and materials. The model is designed as a combination of previously studied and published models for separate phases of the microstructure evolution.
Intrinsic residual microstrains are used to raise the mechanical problem to a larger scale and to model the behavior of complex multilayer films. We have calibrated our model using measurements of SiGe PECVD thin film (cantilever) deflection. The theoretically obtained microstrain curve reproduces very well experimental results. Finally, we have investigated the impact of a process parameter variation on the microstrains. Since the model explicitly includes both process and material parameters, it can readily be used to improve the mechanical behavior of thin films.

2 High-Field Electron Mobility Model for Strained Si Devices

The application of mechanical stress to enhance the carrier mobility in Si has been well established in the last few years. This work probes into the electron conduction in biaxially and uniaxially stressed Si in the non-linear transport regime. The electron behavior has been analyzed for different field directions and stress/strain conditions using full-band Monte Carlo (MC) simulations. An analytical model describing the velocity components parallel and perpendicular to the electric field has been developed. The model includes the effect of strain induced valley splitting and can be applied for arbitrary directions of the electric field. The extension to different field directions has been performed using a Fourier series interpolation and a spherical harmonics interpolation for transport in two and three dimensions, respectively. The model can be implemented in a drift-diffusion based device simulator.

2.1 Introduction

Uniaxially stressed Si, offering larger electron and hole mobilities [8] [9] compared to conventional Si is becoming increasingly accepted by the semiconductor manufacturing industry. Stress causes a deviation of the Si lattice constant from its equilibrium value, thereby modifying the electronic band structure. Mechanical stress in Si can be generated either globally, by growing an epitaxial layer on a relaxed SiGe substrate [10][11][12], by mechanical deformation [13][14], or induced during the processing steps [9][15]. Biaxially strained Si layers grown on relaxed SiGe substrates have shown large enhancements of electron mobility. This method however suffers from several integration issues. There has thus been a growing interest in uniaxially strained Si, which delivers superior mobilities for both electrons and holes.

Strain induced enhancement of the low-field electron mobility can be attributed to two concurring effects. Firstly, inter-valley phonon scattering is reduced due to a decreased number of final available states. Secondly, due to the energy lowering of the Δ_2 valleys, the electrons prefer to occupy this valley and therefore experience a lower in-plane conductivity effective mass. While biaxial tensile strain delivers an energy splitting of around 60 meV per 10% Ge content, uniaxial stress results in around 90 meV of splitting per 1 GPa stress. A model for the low-field electron mobility in strained Si has been proposed in [16]. It describes the mobility tensor in strained Si layers as a function of the strain. The model includes the effect of strain-induced splitting of the con-

Table 1: Coupling constants for intervalley scattering in Silicon in [10^8 eV/cm]

Type of scattering	g_1	g_2	g_3	f_1	f_2	f_3
Values	0.4716	0.7574	10.42	0.348	2.32	2.32

duction band valleys in Si, inter-valley scattering, doping dependence and temperature dependence.

We present here a systematic study of the electron high-field transport in Si under biaxial and uniaxial stress conditions using full-band Monte Carlo (MC) simulations. A strain dependent empirical model describing the velocity vector as a function of the magnitude and direction of the electric field is presented.

The goal of this work is an analytical description of the velocity characteristics at high electric field. To get a complete mobility model for device simulation, this high-field behavior has to be combined with mobility models incorporating the effects dominant at low driving field, such as impurity scattering and surface roughness scattering. This approach, sometimes referred to as the onion model, starts with a proper expression for the lattice mobility, and adds then the effects of impurity scattering, surface reduction, and finally velocity saturation. Using this notion, the presented high-field model can be combined with any low-field model incorporating the aforementioned scattering effects. Note that effects such as surface reduction and velocity saturation are dominant in different device regions. Surface roughness scattering is most effective for carriers confined in a channel, where the driving field is low. On the other hand, high driving fields occur in the pinch-off region, where carriers are no longer quantized in sub-bands, but behave bulk like. Indeed, the transition region of moderate driving fields, where a significant fraction of carriers is still quantized and already moderate carrier heating takes place, the error of this onion type model may be somewhat higher than in the low-field and high-field limits.

2.2 High-Field Electron Transport in Strained Silicon

The velocity-field characteristics needed for the development of the analytical model have been obtained by full band Monte Carlo simulations. In this section some peculiarities of the velocity-field characteristics in strained Si are discussed.

The band structure for strained Si was calculated using the empirical pseudopotential method [17]. MC simulations have been performed and the results calibrated

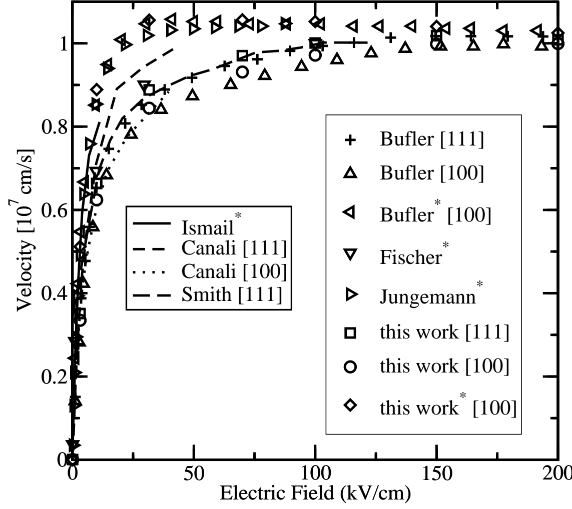

Figure 7: Comparison of electron velocity versus field characteristics in unstrained and strained (*) Si on $Si_{0.7}Ge_{0.3}$ for [100]/[111] field directions.

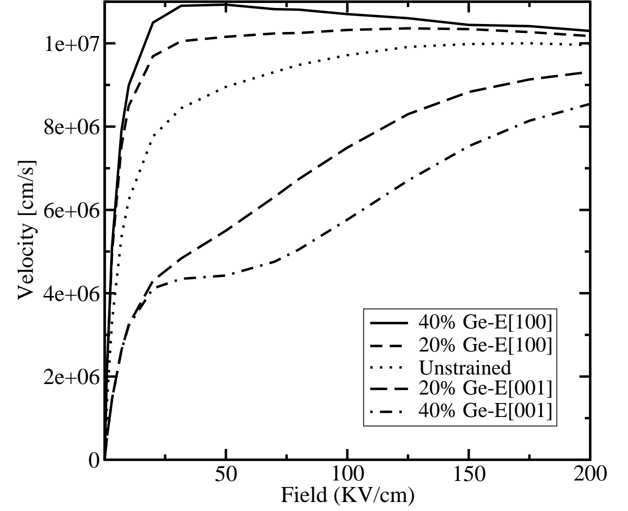

Figure 8: Electron velocity in strained Si on SiGe with Ge content as a parameter for field along [100] and [001] directions.

with the existing theoretical and experimental data. It has been previously reported that the enhancement of the bulk low-field electron mobility saturates at around 1.7 [16]. In order to maintain the desired mobility enhancement, the g-type coupling constants had to be decreased by 6% and the f-type coupling constant increased by 16%, as compared to the original values proposed by Jacoboni [18]. In addition, it was required to adjust the acoustic deformation potential from its original value of 8.9 eV [19] to 8.5 eV. The effect of impact ionization has been neglected for the field regime investigated.

Fig. 7 presents the velocity-field characteristics for unstrained and strained Silicon for different field directions as obtained from MC simulations. Also displayed are the results from Bufler [20], Canali [21], Smith [22], Fischer [23], and Ismail [24]. The simulation results agree well with measured data from Smith for the [111] field direction and with Canali for the [100] field direction for the unstrained case and with [19], [20], and [24] for the strained case.

Fig. 8 depicts the velocity-field characteristics as obtained from MC simulations for biaxially strained Si grown on a relaxed SiGe substrate for different Ge content and field along the in-plane ([100]) and out-of-plane ([001]) direction, respectively. The total velocity increases with strain for a field along the [100] direction and it decreases for a field along the [001] direction. For the in-plane electric field([100]) the electron velocity shows a region of small negative differential mobility. The velocity-field characteristics for field along [001] direction exhibit an untypical form for high strain levels.

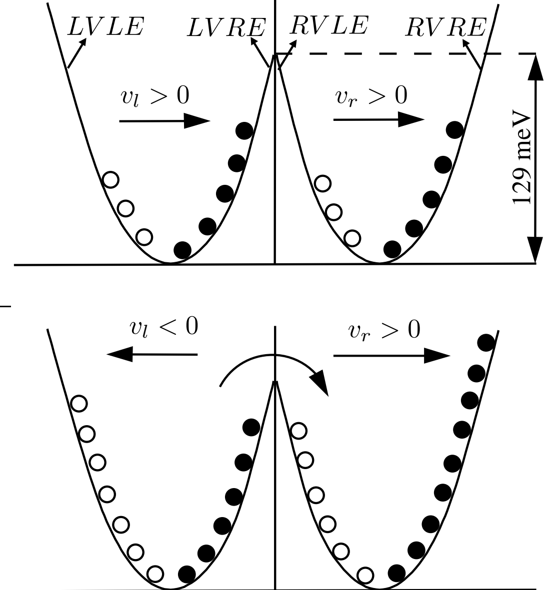

Figure 9: Asymmetric electron populations of the double valley close to the equilibrium state (top) and at high-field (bottom). Solid circles indicate electrons with positive group velocity. Open circles refer to electrons with negative group velocity. LVLE: left valley left edge; LVRE: left valley right edge; RVLE: right valley left edge; RVRE: right valley right edge

This phenomenon can be explained by the repopulation of valleys induced by the field.

For field along [001] direction the Δ_2-valleys are lowered in energy with increasing strain and have the longitudinal mass in the field direction. These valleys are

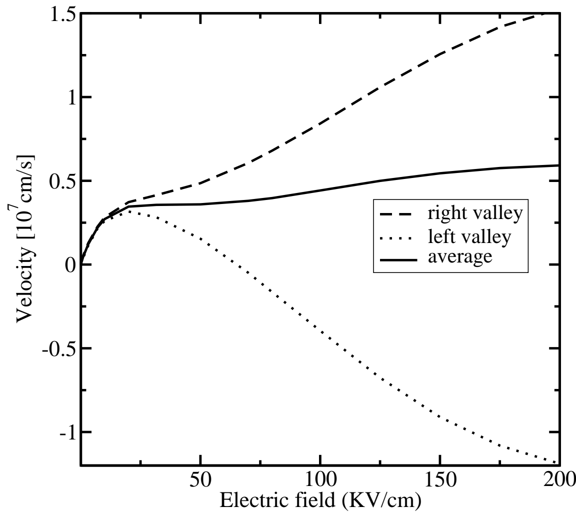

Figure 10: Velocity vs field for left valley and right valley together with the average valley velocity, computed as explained in the text.

located at a scaled distance of 0.85 and 1.15 from the center of the first Brillouin zone and are separated by an energy barrier of 129 meV at the X-point (Fig. 9). The average velocity in the left and right valley and also the average of these velocities are shown in Fig. 10. For low-fields, electrons in both valleys are slightly displaced with respect to the valley minima. This results in the initial velocity increase for both valleys shown in Fig. 10. However, as the field increases, electrons in both valleys gain energy, and electrons from one valley can surpass the energy barrier and drift to the valley in the next Brillouin zone. As sketched in Fig. 9, there are more electrons populating the right side of the double valley than the left side, giving rise to a slight increase in average velocity. If only the left valley is considered, there are more electrons populating the left edge of the single valley resulting in a negative valley velocity, as shown in Fig. 10.

2.3 Analytical High Field Velocity Model

In general, high field mobility is modeled differently for the drift-diffusion and the hydrodynamic transport model. In the former case mobility is modeled as a function of the driving force, whereas in the latter case a dependence on the carrier temperature is usually assumed. To describe nonlocal transport effects occurring in aggressively scaled devices a mobility model for the hydrodynamic framework would be desirable. Such a model could include a three-valley band structure and deal with arbitrary strain conditions. It would capture the essential physics of multi-valley transport under a spatially rapidly varying electric field profile. However, one problem is complexity. A nonlinear system of nine unknowns, namely the valley populations, valley velocities and valley temperatures, has to be solved numerically. The peculiar shape of the $v(E)$ curves for field along [001] direction would pose an additional problem, requiring some empirical fitting. The strain and field dependences of the energy relaxation times for each valley would require careful modeling in order to obtain realistic carrier temperatures and, consequently, realistic valley population. In the past, multi-valley transport models have also been devised for compound semiconductors [25]. As a matter of fact, it seems that such multi-valley transport models with separate carrier gases for each valley have never found application in commercial or academic device simulators.

To find a trade-off between physical rigor and an acceptable level of model complexity we abstained from the multi-valley approach and pursued a more empirical approach, where analytical expressions for the velocity-field characteristics are directly fitted to bulk Monte Carlo data.Our model is restricted to such strain conditions where only one pair of X-valleys is shifted and four valleys remain degenerate. These conditions include biaxial stress and uniaxial stress applied along the $\{100\}$ axes of Si. Another condition resulting in a separation of the Δ_2 and Δ_4 valleys is uniaxial stress in the $\{110\}$ direction. Depending on the stress applied, the strain tensor can be calculated using Hook's law and the strain-induced valley splitting can be obtained from linear defomrmation potential theory [26].

$$\Delta\varepsilon^{(i)} = \Xi_d\,(\varepsilon_{11} + \varepsilon_{22} + \varepsilon_{33}) + \Xi_u\,\varepsilon_{ii}\,, \quad i = 1,2,3 \quad (5)$$

The values of the deformation potentials Ξ_d and Ξ_u have been identified as 1.1 eV and 9.29 eV, respectively. The value of Ξ_u has been extracted from the numerical band structure data. Equation (5) shows that the valley splitting depends only on the diagonal elements of the strain tensor. The proposed mobility model is thus applicable, if two diagonal elements are equal, $\epsilon_{11} = \epsilon_{22} \neq \epsilon_{33}$.

To develop a clear understanding of the model, we have to consider three different coordinate systems.

1. The principal coordinate system has to be oriented such that the unit vectors $\vec{e}_1$, $\vec{e}_2$, and $\vec{e}_3$ correspond to the [100], [010], and [001] crystallographic directions, respectively. In this system the Δ_4-valleys are aligned along the [100] and [010] directions, whereas the Δ_2- valleys are aligned along the [001] direction.

2. The unit vectors $\vec{e}_x$, $\vec{e}_y$, and $\vec{e}_z$ constitute the device coordinate system. In this system the device geometry is defined. For performing device simulations it is essential to transform all transport parameters into this coordinate system.

3. A polar coordinate system is employed, comprising a unit vector along the field direction, $\vec{e}_E = \vec{E}/|E|$, and two orthogonal vectors $\vec{e}_\theta$ and $\vec{e}_\varphi$. The polar axis is aligned with the [001] direction. In terms of the polar angle θ and the in-plane (azimuth) angle φ, the unit vectors are defined as follows.

$$\vec{e}_E = \begin{pmatrix} \sin(\theta)\cos(\varphi) \\ \sin(\theta)\sin(\varphi) \\ \cos(\theta) \end{pmatrix},$$
$$\vec{e}_\theta = \frac{\partial \vec{e}_E}{\partial \theta}, \qquad \vec{e}_\varphi = \frac{1}{\sin(\theta)} \frac{\partial \vec{e}_E}{\partial \varphi} \tag{6}$$

2.3.1 Parallel Velocity Model

A widely used model describing the electron high field behavior in unstrained Si has been adopted [27].

$$v_E = \frac{2\mu_0 E}{1 + \left[1 + \left(\frac{2\mu_0 E}{v_s}\right)^\beta\right]^{1/\beta}} \tag{7}$$

Here μ_0 denotes the low field mobility and v_s the saturation velocity. The parameter β describes the transition from low to high fields. Although (7) can describe the high field behavior in unstrained Si, it can neither account for the small negative differential mobility nor the velocity plateau seen in strained Si (Fig. 8) .

Table 2: Parameter values for the parallel velocity component v_E in unstrained Si

Parameter	Units	E [100] E [001]	E [110] E [101]	E [11$\sqrt{2}$]
v_{s1}	[10^7 cm/s]	1.026	1.058	1.042
β_1	[1]	1.085	1.2475	1.273

We thus use an expression previously suggested in [28], which can handle all types of velocity-field characteristics resulting from the MC simulations performed.

$$v_E = \frac{2\mu_{EE} E}{1 + \left[1 + \left(\frac{2\mu_{EE} E}{v_s(1-\xi)}\right)^\beta\right]^{1/\beta}} + v_s \xi \frac{(E/\eta)^\gamma}{1 + (E/\eta)^\gamma} \tag{8}$$

Here μ_{EE} denotes the low-field mobility in the field direction, obtained by projection of the low-field mobility tensor as $\mu_{EE} = \vec{e}_E^T \cdot \mu_0 \cdot \vec{e}_E$. The additional term incorporated in (8) models the velocity kink shown in Fig. 8. The relevance of the parameter ξ is twofold: It accounts for the velocity plateau occurring approximately at $v_s(1-\xi)$ and also signifies the small negative differential mobility occurring in strained Si for higher strain levels. The parameters η and γ are fit parameters.

All parameters depend on the strain-induced valley splitting, $\Delta\varepsilon = \varepsilon(\Delta_2) - \varepsilon(\Delta_4)$. The following empirical expressions were assumed.

$$v_s = v_{s1} + v_{s2} \cdot \Delta\varepsilon \tag{9}$$
$$\beta = \beta_1 + \beta_2 \cdot \Delta\varepsilon \tag{10}$$
$$\eta = \eta_1 + \eta_2 \cdot \Delta\varepsilon \tag{11}$$
$$\gamma = \gamma_1 + \gamma_2 \cdot \Delta\varepsilon \tag{12}$$
$$\xi = \frac{(\Delta\varepsilon/\xi_1)}{1 + (\Delta\varepsilon \cdot \xi_2/\xi_1)^2} \tag{13}$$

For all parameters except ξ, a linear dependence was found to be sufficient. The parameter ξ was modeled by the rational expression in (13). The parameters v_{si}, β_i, η_i, γ_i, ξ_i where $i = 1, 2$, are constants for a particular field direction. We have chosen the three high symmetry directions [100], [110], and [001] and two additional directions [101] and [11$\sqrt{2}$]. The parameters in (9) to (13) have been obtained using the optimization framework of MATLAB [29]. A multidimensional unconstrained nonlinear minimization (Nelder-Mead) technique was adopted for obtaining the parameter set.The optimized values of the parameters for these field directions are listed in Tables 1, 2 and 3. It should be noted that the optimization technique is sensitive to the initial conditions of the parameters and therefore a small variation in the initial conditions can result in a slightly varied parameter set.

Fig. 11 shows the $v_E(E)$ characteristics for a 1GPa stressed (along [001]) Si layer for field along [100] and [001] directions, respectively. Application of uniaxial compressive stress enhances the velocity along [100] direction in the same way as biaxial tensile strain does. Conversely, applying uniaxial tensile stress results in an enhanced velocity along [001] direction.

2.3.2 Perpendicular Velocity Model

For the cases where the field is not oriented in a high symmetry direction, it is observed that an electron velocity perpendicular to the field direction develops. Fig. 12 shows the perpendicular electron velocity, $\vec{v}_\theta$ for field along the [101] direction for increasing stress level, as obtained from MC simulations. The component $\vec{v}_\theta$, although small for low stress levels, has a significant magnitude for intermediate field regimes. For symmetry reasons, the velocity component in the $\vec{e}_\varphi$ direction vanishes for all five sample directions.

The perpendicular velocity component vanishes for fields along the [100], [110] and [001] directions. For the field directions [101] and [11$\sqrt{2}$], the normal velocity can be expressed in terms of v_E and v_3.

$$v_\perp = v_E - \sqrt{2} v_3 \tag{14}$$

After fitting v_E, the component v_3 is fitted using an expression similar to (8)

$$v_3 = \frac{\sqrt{2}\mu_{33}E}{1+\left[1+\left(\frac{2\mu_{33}E}{v_s(1-\xi)}\right)^{\beta}\right]^{1/\beta}} + \frac{v_s}{\sqrt{2}}\xi\frac{(E/\eta)^{\gamma}}{1+(E/\eta)^{\gamma}} \tag{15}$$

To ensure the correct low-field behavior, $v_3 = \mu_{33}E_3$, the magnitude of the electric field E in the first term in (8) has to be replaced by $E_3 = E/\sqrt{2}$ to obtain (15). The correct high-field limit is introduced by replacing v_s in (8) by $v_{3,s} = v_s/\sqrt{2}$. For the unstrained case the values of the parameters β and v_s are identical with those listed in Table 1. The fitting of the parameters in (15) is performed such that the error in $v_\perp$ is minimized. The values of the other parameter for the field directions [101] and [11$\sqrt{2}$] are listed in Table 4.

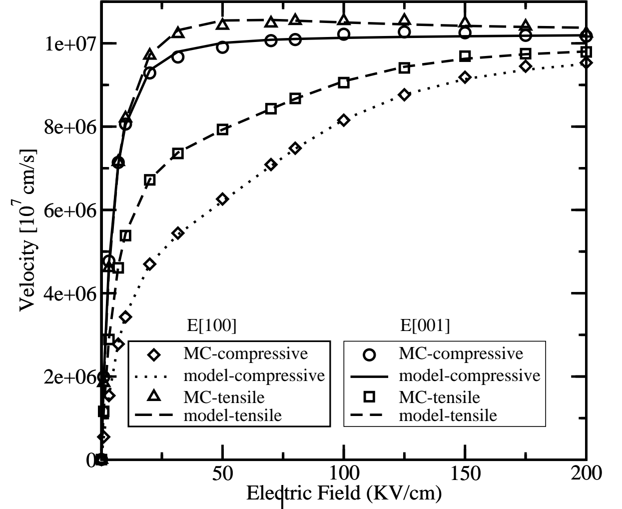

Figure 11: Parallel electron velocity component versus field for Si under uniaxial stress (1GPa) along [001] and field along [100] and [001] directions, respectively.

2.3.3 Total Velocity for Fixed Field Direction

The total electron velocity vector is obtained by addition of the two components.

$$\vec{v}_t = v_E\vec{e}_E + v_\theta\vec{e}_\theta \tag{16}$$

where $\vec{e}_E$ and $\vec{e}_\theta$ are the unit vectors parallel and perpendicular to the field direction. Fig. 13 shows a comparison of the velocity components and total velocity for -3GPa stress for field along the [11$\sqrt{2}$] direction, as obtained from MC simulations and the analytical model. The results from the model are in good agreement with the MC data.

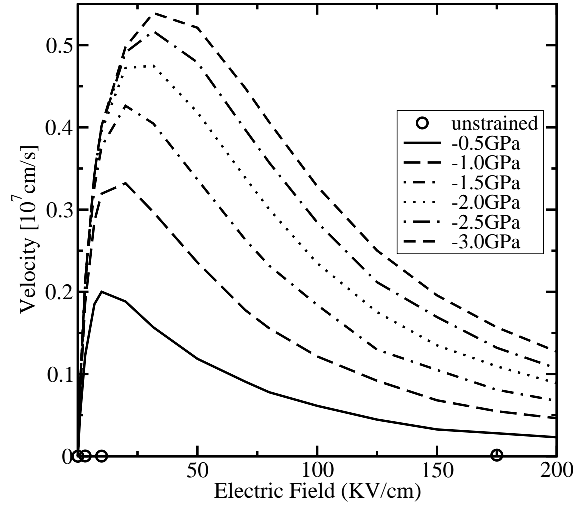

Figure 12: Perpendicular velocity versus field for Si under increasing uniaxial stress along [001] and field along [101].

2.3.4 Total Velocity for Arbitrary Field Direction

The velocity-field characteristics can be extended to other field directions using a spherical harmonics interpolation.

$$\Phi(\theta,\varphi) = \sum_{l=0}^{\infty}\sum_{m=0}^{l} a_{lm}P_l^m[\cos(\theta)]\cos(m\varphi) \tag{17}$$

Here, Φ is the function to be interpolated, a_{lm} denote the expansion coefficients and P_l^m are the associated Legendre polynomials. From the symmetry properties $\Phi(\theta,\varphi+\pi/2) = \Phi(\theta,\varphi)$ and $\Phi(\theta+\pi,\varphi) = \Phi(\theta,\varphi)$ it follows that l must be even and $m = 4n$. Truncating (17) after the 4th order yields

$$\Phi(\theta,\varphi) = a_{00}P_0^0(\chi) + a_{20}P_2^0(\chi) + a_{40}P_4^0(\chi) + \\ + a_{44}P_4^4(\chi)\cos(4\varphi) \tag{18}$$

where $\chi = \cos(\theta)$. Evaluating (18) for field directions [100], [110], [001], [101] and [11$\sqrt{2}$] gives

$$\Phi_{100} = a_{00} - \frac{1}{2}a_{20} + \frac{3}{8}a_{40} + 105a_{44} \tag{19}$$

$$\Phi_{110} = a_{00} - \frac{1}{2}a_{20} + \frac{3}{8}a_{40} - 105a_{44} \tag{20}$$

$$\Phi_{001} = a_{00} + a_{20} + a_{40} \tag{21}$$

$$\Phi_{011} = a_{00} + \frac{1}{4}a_{20} - \frac{13}{32}a_{40} + \frac{105}{4}a_{44} \tag{22}$$

$$\Phi_{11\sqrt{2}} = a_{00} + \frac{1}{4}a_{20} - \frac{13}{32}a_{40} - \frac{105}{4}a_{44} \tag{23}$$

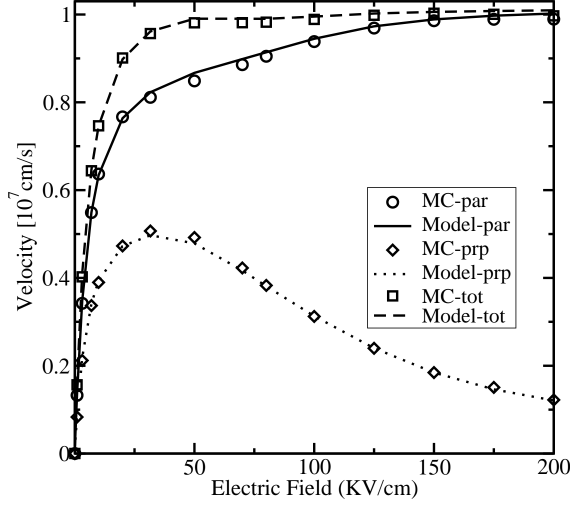

Figure 13: Parallel (par) and perpendicular (prp) velocity components and total (tot) velocity versus field for Si under uniaxial stress (-3GPa) along [001] and field along [$11\sqrt{2}$].

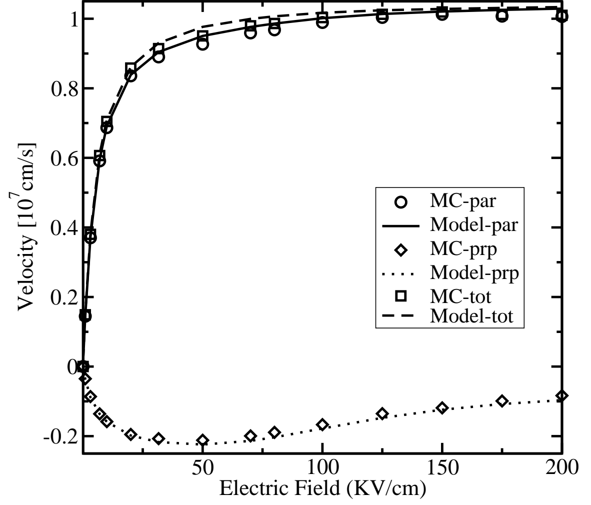

Figure 14: Interpolated parallel (par) electron velocity components and perpendicular (prp) velocity and the total (tot) velocity versus field for Si under uniaxial stress (3GPa) along [001] and field along [111].

To determine the four coefficients from the overdetermined system (19) to (23), we solve (19) to (21) exactly and minimize

the error in (22) and (23).

$$a_{00} = \frac{1}{3}(\Phi_{100} + \Phi_{110} + \Phi_{001}) - \frac{7}{12}a_{40} \quad (24)$$

$$a_{20} = \frac{1}{3}(2\Phi_{001} - \Phi_{100} - \Phi_{110}) - \frac{5}{12}a_{40} \quad (25)$$

$$a_{40} = \frac{8}{35}(\Phi_{100} + \Phi_{110} + 2\Phi_{001} - 2\Phi_{011} - 2\Phi_{11\sqrt{2}}) \quad (26)$$

$$a_{44} = \frac{1}{210}(\Phi_{100} - \Phi_{110}) \quad (27)$$

It was found that interpolation of the quantities $\Phi = v_E^2$ and $\Phi = v_3^2$ gives good agreement to MC data.

Fig. 14 show a comparison of the velocity components and the total velocity as obtained from the interpolation and MC simulations for field along the [111] direction for uniaxial tensile stressed Si. It can be seen that tensile stress causes the parallel and perpendicular velocities to have opposite signs.

Simplification to Two-Dimensional Simulation Domains

For a given value of φ, the quantity Φ in (18) can alternatively be interpolated using a polynomial.

$$\Phi(\theta) = b_0 + b_2\cos^2(\theta) + b_4\cos^4(\theta) \quad (28)$$

Considering the special case of transport in the <010> plane ($\varphi = 0$), we can write the equation system

$$\Phi_{100} = b_0 \quad (29)$$

$$\Phi_{101} = b_0 + \frac{b_2}{2} + \frac{b_4}{4} \quad (30)$$

$$\Phi_{001} = b_0 + b_2 + b_4 \quad (31)$$

which gives the coefficients

$$b_2 = -3\Phi_{100} + 4\Phi_{101} - \Phi_{001} \quad (32)$$

$$b_4 = 2\Phi_{100} - 4\Phi_{101} + 2\Phi_{001} \quad (33)$$

Similarly, for transport in a < $\bar{1}$10> plane ($\varphi = \frac{\pi}{4}$), we have

$$\Phi_{110} = b_0 \quad (34)$$

$$\Phi_{11\sqrt{2}} = b_0 + \frac{b_2}{2} + \frac{b_4}{4} \quad (35)$$

$$\Phi_{001} = b_0 + b_2 + b_4 \quad (36)$$

giving

$$b_2 = -3\Phi_{110} + 4\Phi_{11\sqrt{2}} - \Phi_{001} \quad (37)$$

$$b_4 = 2\Phi_{110} - 4\Phi_{11\sqrt{2}} + 2\Phi_{001} \quad (38)$$

The quantities to be interpolated are $\Phi = v_E^2$ and $\Phi = v_3^2$. Note that for a field in [100] and [110] direction, the component v_3 vanishes. Therefore, for this quantity the calculation of the coefficients simplifies because $\Phi_{100} = \Phi_{110} = 0$. Using the relations (32) and (33) for the $\varphi = 0$ plane and (37) and (38) for the $\varphi = \pi/4$ plane, the velocity components can be interpolated.

2.4 Implementation Issues

The present model has been derived for a uniform electric field, $\vec{E}$. To apply it in a drift diffusion based device simulator, the electric field in the model has to be replaced by an appropriately defined driving force, $\vec{F}_n$. Typical definitions of the driving force employed in practical devices simulators are the electric field component along the current density vector or the gradient of the quasi Fermi level.

For the two-dimensional cases described in Section IV.A, only one angle has to be determined. With the constant, two-dimensional vector $\vec{e}_3$ denoting the [001] direction, one obtains for the polar angle

$$\cos^2(\theta) = \frac{(\vec{F}_n \cdot \vec{e}_3)^2}{\vec{F}_n \cdot \vec{F}_n}. \tag{39}$$

The involved vectors are two-dimensional and specified in the device coordinate system.

In order to implement the model in conventional two-dimensional drift-diffusion based device simulators, the mobility is needed at the mid-point of the grid edge. By assuming a suitably interpolated value of the normal component of the driving force, the mobility tensor in the polar coordinate system can be written as

$$\widehat{\mu} = \begin{pmatrix} \mu_{EE} & 0 \\ 0 & \mu_\theta \end{pmatrix} \tag{40}$$

with the mobility components,

$$\mu_{EE} = \frac{v_t(\vec{F_n}) \cdot \hat{\vec{F}}}{|\vec{F}|} \quad \mu_\theta = \frac{v_t(\vec{F_{n\perp}}) \cdot \hat{\vec{F}}}{|\vec{F}|}. \tag{41}$$

Here $F_{n\perp}$ denotes the perpendicular driving force component and $\hat{\vec{F}}$ is a unit vector. In analogy with the diagonal form of the low-field mobility tensor, we assume that the mobility tensor remains diagonal for high-fields. The mobility along the grid edge, ζ is then determined by taking the projection of the mobility tensor.

$$\mu_{\zeta\zeta} = \zeta^T \begin{pmatrix} \mu_{EE} & 0 \\ 0 & \mu_\theta \end{pmatrix} \zeta \tag{42}$$

2.5 Conclusion

A comprehensive study of the electron high-field transport in strained Si for different field directions and stress conditions has been performed using full-band MC simulations. A phenomenological approach to calculate the mobility tensor at high electric fields has been proposed. The structure of the proposed high-field model can be summarized as follows:

1. For five given field directions the parallel components $v_E(E)$ of the velocity vectors are empirically fitted. These five chosen directions form a spherical triangle.

2. For two out of the five field directions a normal velocity component develops. The normal components $v_\theta(E)$ in the direction $\vec{e}_\theta$ are also empirically fitted. For all field directions chosen, the normal component along the $\vec{e}_\varphi$ direction will vanish.

3. The velocity vector for the actual field direction is obtained from the velocity vectors for the sample directions by means of interpolation.

4. In the crystallographic system the mobility tensor is assumed to be diagonal. The three diagonal elements are determined from the velocity and field vectors.

5. The mobility tensor is transformed to the device coordinate system by a unitary transformation.

This approach seems to be more suitable for device simulation purpose than a more physics based model due to the inherent complexities discussed in Section III. The presented model is applicable for all stress conditions which cause the X-valleys to split into two-fold degenerate Δ_2-valleys and four-fold degenerate Δ_4-valleys. It has been extended to arbitrary field directions using an interpolation technique. The path of implementing the model in drift-diffusion based device simulator is briefly outlined.

Table 3: Parameter values for the parallel velocity component v_E for $\Delta\epsilon < 0$

Parameter	Units	E [100]	E [001]	E[110]	E [101]	E [11$\sqrt{2}$]
v_{s2}	$[10^5 \text{ cms}^{-1}\text{eV}^{-1}]$	-5.5691	33.731	1.4988	11.739	11.067
β_2	$[\text{eV}^{-1}]$	-0.33235	-5.2879	0.22885	-0.30235	-0.39907
ξ_1	[eV]	0.37994	-0.22859	0.45615	-0.84676	-0.76303
ξ_2	[1]	1.6239	1.0333	1.5468	6.3401	4.7611
η_1	$[10^4 \text{ Vcm}^{-1}]$	2.1254	6.3369	0.6651	4.2133	5.4664
η_2	$[10^5 \text{ Vcm}^{-1}\text{eV}^{-1}]$	-1.13	-2.748	-0.86273	-2.0402	-1.5317
γ_1	[1]	1.3707	2.6051	1.3869	2.4453	3.4612
γ_2	$[\text{eV}^{-1}]$	-0.73185	-6.3392	0.61215	-13.938	-7.1773

Table 4: Parameter values for the parallel velocity component v_E for $\Delta\epsilon > 0$

Parameter	Units	E [100]	E [001]	E [110]	E [101]	E [11$\sqrt{2}$]
v_{s2}	$[10^5 \text{ cms}^{-1}\text{eV}^{-1}]$	-20.608	10.822	-14.625	2.2239	3.5825
β_2	$[\text{eV}^{-1}]$	0.472	0.5135	0.21785	-0.41762	-0.27011
ξ_1	[eV]	0.47701	-0.29814	1.0876	-1.3718	1.9381
ξ_2	[1]	3.1569	2.1639	-8.5962	-4.2752	5.5323
η_1	$[10^4 \text{ Vcm}^{-1}]$	7.6075	3.7613	5.8913	0.25071	1.1382
η_2	$[10^5 \text{ Vcm}^{-1}\text{eV}^{-1}]$	1.471	2.7214	1.3928	0.92226	-0.19962
γ_1	[1]	3.815	1.163	4.7754	1.4471	0.7351
γ_2	$[\text{eV}^{-1}]$	2.9118	4.8595	5.2425	0.14618	5.2995

Table 5: Parameter values for the [001] velocity component v_3

Parameter	Units	E [101] $\Delta\epsilon < 0$	E [101] $\Delta\epsilon > 0$	E [11$\sqrt{2}$] $\Delta\epsilon < 0$	E [11$\sqrt{2}$] $\Delta\epsilon > 0$
v_{s2}	$[10^6 \text{ cms }^{-1}\text{eV}^{-1}]$	4.0975	2.8429	3.53	3.4858
β_2	$[\text{eV}^{-1}]$	-1.7085	-0.22173	-1.7571	-0.26191
ξ_1	[eV]	-0.16917	-0.3354	-0.17293	-0.36817
ξ_2	[1]	0.75896	-1.9529	0.76209	2.2891
η_1	$[10^4 \text{ Vcm}^{-1}]$	3.9982	5.9335	4.223	6.5366
η_2	$[10^5 \text{ Vcm}^{-1}\text{eV}^{-1}]$	-2.2147	1.9583	-2.1683	1.8587
γ_1	[1]	1.8204	1.9209	2.0921	1.668
γ_2	$[\text{eV}^{-1}]$	-4.6684	3.5664	-3.5816	5.4713

3 Analysis of Hole Transport in Arbitrarily Strained Germanium

Full-band Monte Carlo simulations are performed to study the properties of hole transport in bulk Germanium under general strain conditions. The band structures are calculated with the empirical non-local pseudopotential method. For Monte Carlo simulations acoustic and optical phonon scattering as well as impact ionization are taken into account. Results for biaxially strained Ge grown on a $[001]$ oriented $\mathrm{Si}_{1-x}\mathrm{Ge}_x$ substrate and for uniaxial compressive stress in $[110]$ exhibit a high mobility enhancement. These results are compared to experimental and theoretical results from literature.

3.1 Introduction

The history of semiconductor device technology started with Germanium as the preferred material, while today the mainstream semiconductor technology is centered around Silicon. Over decades performance gains and increasing integration density of CMOS devices where successfully obtained by down-scaling, a process which is getting more and more cost intensive as it is pushed closer to some principal physical limits. So the demand for alternatives to down-scaling rises, leading to new opportunities for Ge, particularly motivated by its higher carrier mobility compared to Si. The hole mobility, being approximately four times higher than in Si, can be further enhanced by stress engineering. This has been shown in previous experimental and theoretical works for biaxially strained Ge epitaxially grown on a $[001]$ oriented $\mathrm{Si}_x\mathrm{Ge}_{1-x}$ substrate [30][31][32]. In this work we analyze hole transport properties of arbitrarily stressed/strained Ge by means of full-band Monte Carlo simulation (FBMC).

3.2 Band Structure Calculation

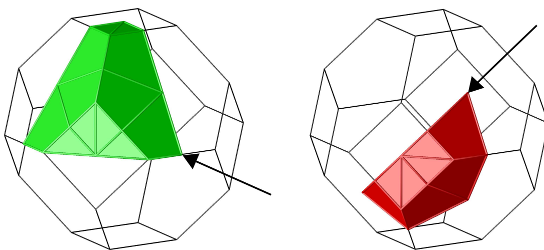

Figure 15: Irreducible wedge for stress applied in $[110]$ and in $[111]$ direction.

For FBMC simulations a numerical representation of the band structure in the unit cell of the reciprocal lattice, the so-called *Brillouin zone*, is used to capture the dependence of the carrier energy on the wave vector. Because of symmetry only a part of the Brillouin zone - the *irreducible wedge* - has to be considered for band structure calculation. The volume of the irreducible wedge is determined by the number of symmetry elements $\mathrm{P}(\Gamma)$ at the center of the Brillouin zone of the strained lattice via $\Omega_{\mathrm{irred}} = \Omega_{\mathrm{BZ}}/\mathrm{P}(\Gamma)$. For the diamond type lattice of relaxed Ge $\mathrm{P}(\Gamma)$ is 48, for stress along $\langle 100\rangle$, $\langle 111\rangle$, and $\langle 110\rangle$, as shown in Fig. 15, $\mathrm{P}(\Gamma)$ is 16, 12, and 8, respectively, while for stress along arbitrary direction the lattice is invariant only to inversion, thus $\mathrm{P}(\Gamma) = 2$.

The empirical non-local pseudopotential method (EPM) [33] is generalized to arbitrary stress/strain conditions to calculate the band structures of Ge. For discretization of the band-structure an unstructured tetrahedral mesh is used. Mesh refinement guarantees high resolution around the band minima, while a relatively low total number of mesh elements is maintained [34].

Stress modifies the band structure of a semiconductor. As a consequence the band gap changes, a splitting between light hole and heavy hole band is introduced and also the splitoff band is altered. The band splitting reduces the density of states in the low energy regime and suppresses interband scattering. This effect and the change of the effective masses cause the observed mobility gain. Fig. 18(a) shows the energy splitting between the splitoff band and the valence band edge and Fig. 3.2 the heavy/light hole band splitting energies of biaxially strained Ge grown on a $[001]$ oriented $\mathrm{Si}_{1-x}\mathrm{Ge}_x$ substrate as a result of EPM calculation [33]. For higher compressive strain levels than shown the heavy/light hole band splitting saturates [30]. Fig. 17(a) depicts the energy splitting between the splitoff band and the valence band edge and Fig. 17(b) the heavy/light hole band splitting energies of compressive stressed Ge in [110] direction. The splitting energy rises almost linearly with compressive stress in $[110]$ direction for the shown range of pressure.

3.3 The Vienna Monte Carlo Simulator

The VIENNA MONTE CARLO SIMULATOR (VMC) [35] offers simulation algorithms for both bulk semiconductors and one-dimensional devices based on analytical and full-band models. Additionally, a fast zero-field algorithm is included [36]. VMC provides a mature set of scattering models including phonon scattering, ionized impurity scattering, alloy scattering, and impact ionization. For full-band simulation phonon scattering models with constant matrix elements are used[37]. In this formulation the scattering rates are proportional to the density of states, which is calculated from the band structure. The coupling constants for acoustic and optical phonon

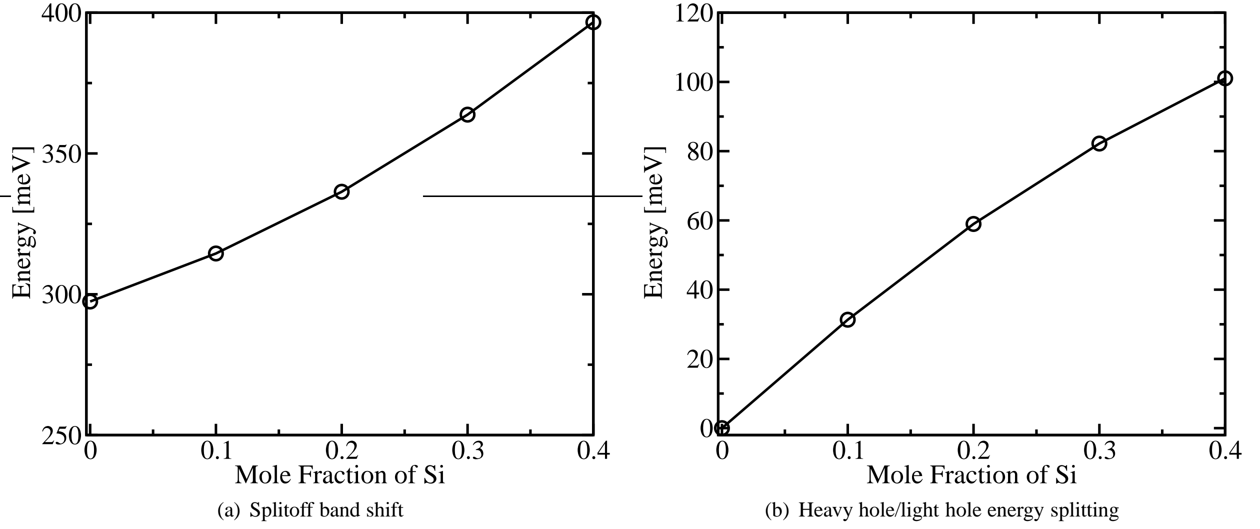

(a) Splitoff band shift

(b) Heavy hole/light hole energy splitting

Figure 16: Splitoff band shift and heavy hole and energy splitting of heavy hole/light hole bands in strained Germanium grown on a Si_xGe_{1-x} layer.

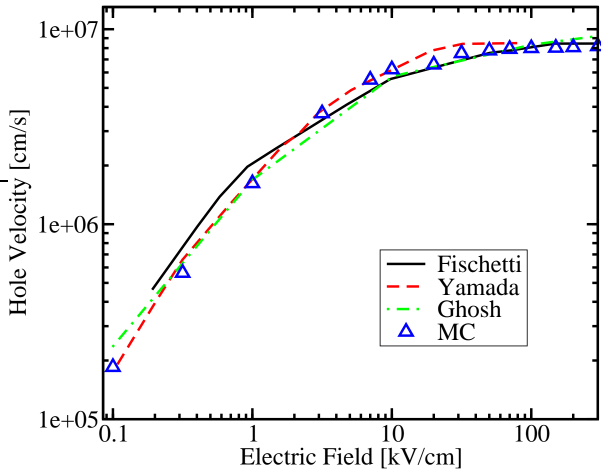

Figure 19: Hole velocity versus field in [100] direction for relaxed Ge compared to results from literature. [30][38]

scattering, as well as the optical phonon energy are given in Table 6. These parameters are used for relaxed and for strained Ge.

Impact ionization is modeled with a threshold expression [39]

$$\frac{1}{\tau_{\mathrm{ii}}} = \theta(\epsilon - \epsilon_{\mathrm{th}}) \cdot \mathrm{P} \cdot \left(\frac{\epsilon - \epsilon_{\mathrm{th}}}{\epsilon_{\mathrm{th}}}\right)^{3.5} \tag{43}$$

where θ is the unit step-function, ϵ is the electron energy, ϵ_{th} is a threshold energy, and P is a multiplication factor which determines the softness of the threshold. The parameters are tuned to reproduce reported hole velocity field characteristics [40][38][41] for relaxed Ge, $\epsilon_{\mathrm{th}} = 0.69\mathrm{eV}$ and $\mathrm{P} = 2.0 \cdot 10^{12}\mathrm{s}^{-1}$. For stressed/strained Ge ϵ_{th} is adjusted in dependence on the bandgap change.

Fig. 19 shows the hole velocity field characteristics and Fig. 20 the energy as a function of the electric field in [100] direction for relaxed Ge. These results are compared to values from literature and show good agreement.

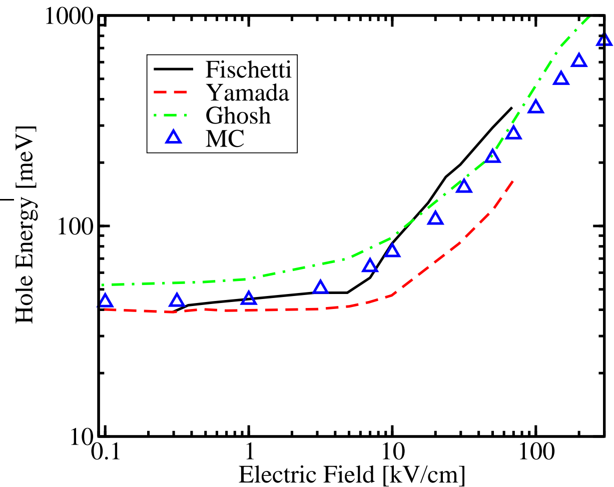

Figure 20: Hole energy versus field in [100] direction for relaxed Ge compared to results from literature. [30][38]

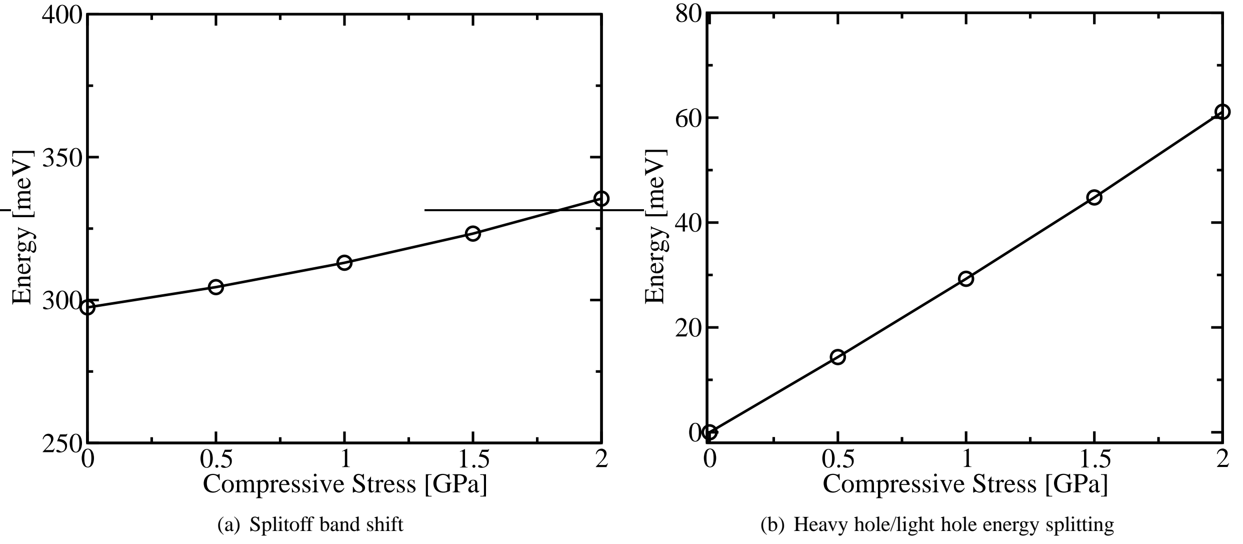

(a) Splitoff band shift (b) Heavy hole/light hole energy splitting

Figure 17: Splitoff band shift and heavy hole and energy splitting of heavy hole/light hole bands of stressed Ge with compressive stress in [110] direction.

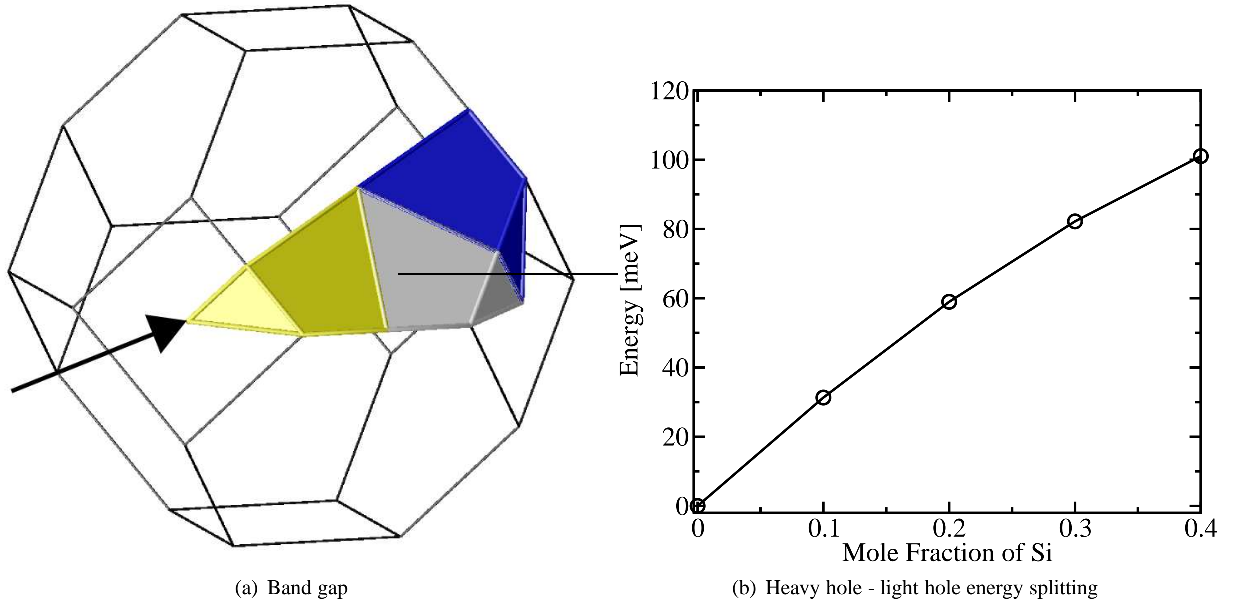

(a) Band gap (b) Heavy hole - light hole energy splitting

Figure 18: Band gap and heavy hole and energy splitting of heavy hole / light hole bands in strained germanium grown on a $\mathrm{Si}_x\mathrm{Ge}_{1-x}$ layer

Table 6: Acoustic deformation potential Δ_{ac}, optical deformation potential Δ_{op} and optical phonon energy $\hbar\omega_{\mathrm{op}}$ for the heavy hole (HH), light hole(LH) and split-off (SO) bands.

Band	Δ_{ac}	Δ_{op}	$\hbar\omega_{\mathrm{op}}$
HH	1.71 eV	9.6e8 eV/cm	37 meV
LH	2.56 eV	9.6e8 eV/cm	37 meV
SO	2.56 eV	9.6e8 eV/cm	37 meV

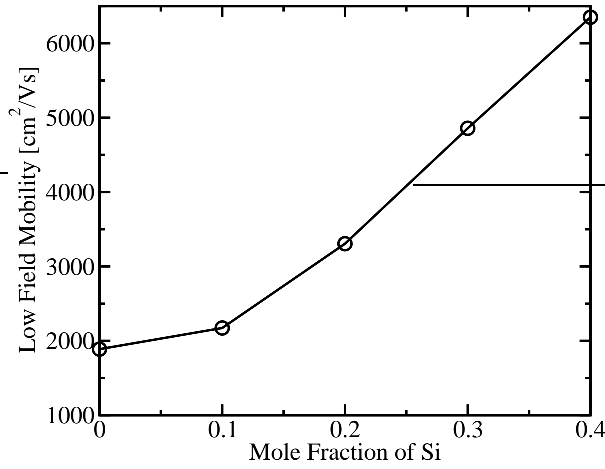

Figure 21: In-plane low field mobility of holes in biaxially compressed Ge grown on a $\mathrm{Si}_x\mathrm{Ge}_{1-x}$ substrate.

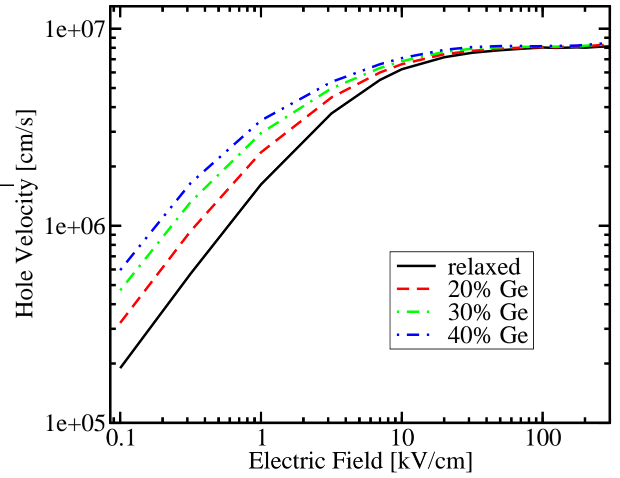

Figure 22: Hole velocity versus electric field for biaxially compressed Ge grown on a $\mathrm{Si}_x\mathrm{Ge}_{1-x}$ substrate in [100] direction.

3.4 Results

Compressively Biaxially Strained Germanium

In this section simulation results for bulk hole transport in biaxially strained Ge epitaxially grown on a $\mathrm{Si}_x\mathrm{Ge}_{1-x}$ substrate with $[001]$ orientation are shown. Since the lattice constant of SiGe is smaller than that of Ge the resulting strain is compressive. Several pMOSFET devices with strained Ge channels based on that technique have been demonstrated [31][32].

Fig. 21 depicts the in-plane low field mobility versus mole fraction of Si in the $\mathrm{Si}_x\mathrm{Ge}_{1-x}$ substrate. For a mole fraction $\mathrm{x} = 0.4$ the low field hole mobility is enhanced by a factor of 3.38 to $6350\ \mathrm{cm}^2/\mathrm{Vs}$. This mole fraction corresponds to biaxial compressive strain of 1.7% in the Ge layer. Fig. 22 shows the velocity field characteristics for field in $[100]$ direction for different Si mole fractions. The highest mobility gain can be observed in the low field regime, while the curves converge in the high field regime.

Uniaxially Strained Germanium

Uniaxial stress technique overcomes a few drawbacks of biaxially strained Ge layers, related to problems of misfit and threading dislocations as well as diffusion. In Si technology CMOS devices with uniaxially stressed channels are already fabricated in large volumes [42]. The stress is hereby introduced by capping layers. In this section results for hole transport in uniaxially stressed Ge with compressive stress in $[110]$ are shown. Although this is a technologically very interesting setup it has been hardly investigated by means of Monte Carlo simulation so far.

Fig. 23 presents the velocity field characteristics for uniaxial stress and field in $[110]$ direction. As for biaxially strain the curves show the highest mobility gain in the low field regime and converge at high electric fields.

Fig. 24 depicts the in-plane hole mobility at low electric field for uniaxial compressive stress. A strong anisotropy with the most pronounced mobility enhancement in stress direction can be observed. A stress level of $1.5\mathrm{GPa}$ enhances the low field mobility by a factor of 2.55 to $4790\ \mathrm{cm}^2/\mathrm{Vs}$. Note that tensile stress instead of compressive stress could also be used for hole mobility enhancement. The most pronounced enhancement is then achieved perpendicular to the applied stress in $[\bar{1}10]$

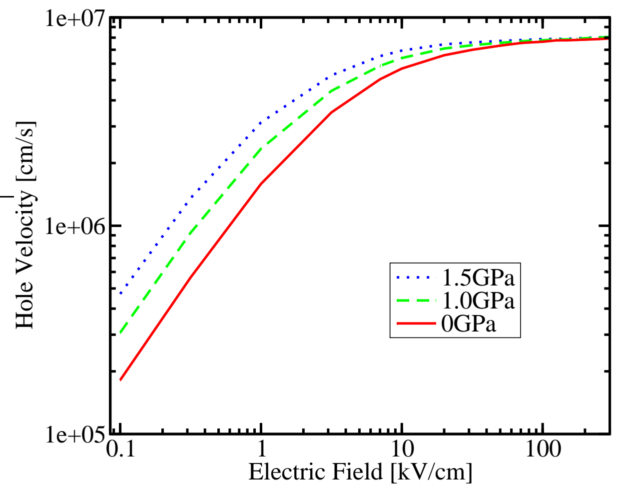

Figure 23: Hole velocity as a function of the electric field in stressed Ge for field and stress in [110] direction.

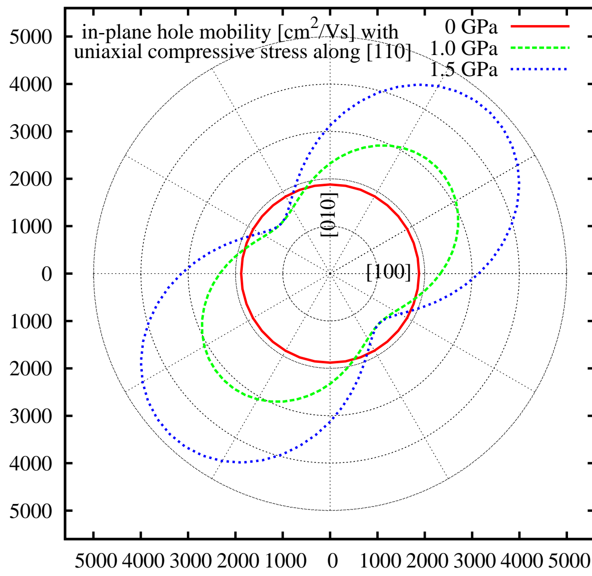

Figure 24: Low field hole mobility in bulk Ge for uniaxial $[110]$ compressive stress.

direction, otherwise the result looks similar as in Fig. 24 for the shown stress levels.

3.5 Conclusion

A full-band Monte Carlo simulator which efficiently handles arbitrary stress/ strain conditions is presented and used to analyse two technologically important applications of stress engineered Ge. It is demonstrated that uniaxial compressive stressed Ge in $[110]$ direction as well as biaxially stressed Ge show high hole mobility enhancement. Therefore, Germanium is indeed a promising material for future applications.

4 Carrier Concentration Dependence of the Mobility in Organic Semiconductors

The charge transport in organic materials as a function of carrier concentration is investigated. An analytical model of the concentration dependent mobility based on the variable hopping range theory is formulated. This model is applied to analyze the discrepancy between the experimental mobilities extracted from FETs and LEDs. The result shows that an exponential density of states (DOS) is a good approximation of the tail states for describing the charge transport in FETs. When applied to the low carrier concentration regime, for example to the LEDs regime, a Gaussian DOS should be assumed.

4.1 Introduction

Organic semiconductors have witnessed a considerable development in recent years, mainly pushed by commercial display applications based on LEDs [43, 44] whose cost and performance are potentially better compared with more conventional solutions. At the same time, interest has also grown for organic thin film transistors (TFTs) [45]. However, the main obstacles to further application of organic transistors are the poor mobility which can be several order of magnitudes smaller than that of conventional semiconductors. Another problem is the lack of knowledge of the microscopic charge transport mechanisms [46]. However, understanding the carrier transport properties in these organic materials is of crucial importance to design and synthesize better materials and to improve device performance.

In organic semiconductors, intramolecular interactions are mainly covalent, but intermolecular interactions are due to much weaker van der Waals and London forces. As a result, the transport bands in organic crystals are much narrower than those of their inorganic counterparts, and the band structure is easily disrupted by disorder in such systems. This disorder causes the formation of localized states in the energy gap. In order to enable a current through the device, charge carriers trapped at the localized states need to escape from these sites. Such a conduction process is entirely determined by the tunneling transitions of carriers between the localized states, provided that the electronic wave functions of the localized states have sufficient overlap. This theory was originally given by Conwell [47] and Mott [48]. A more systematic theory called variable range hopping (VRH) was introduced by Mott in 1968 [49]. The transport properties of organic semiconductors can be well described by VRH theory [50, 51, 52]. The central transport quantity is the mobility μ of the charge carriers and most of the work related to the mobility is on the temperature and electric field dependence. Recently it has been realized that the carrier concentration also plays an important role for the mobility. Experiments show that for a hole-only diode and a FET fabricated from the same conjugated polymer, the mobility could differ up to three orders of the magnitude [53]. This difference can only be explained by taking into account the dependence of mobility on the carrier concentration. Rubel [52] analyzed this problem with the concept of a transport energy ϵ_t, but there is no direct proof for the existence of such transport energy in organic systems. In this paper, we will focus on extending the percolation model based on VRH theory by Vissenberg [54] to explain the discrepancy of measured mobilities in OLEDs and OFETs. An analytical mobility model with a Gaussian DOS function has been obtained. It can explain the relation between the mobility and carrier concentration. Results are in good agreement with experimental data.

4.2 Theory

To calculate the mobility of an organic semiconductor, one can use percolation theory, regarding such system as a random resistor network (network of Miller and Abrahams) [46, 55]. The current flows through the bonds connecting sites in the network. The conductance between the states m and m' can be described as

$$Z_{mm'}^{-1} = Z_0^{-1} \exp\left(-2\alpha \mid R_m - R_{m'} \mid\right) \cdot \\ \cdot \exp\left(-\frac{\mid \epsilon_m - \epsilon_F \mid + \mid \epsilon_{m'} - \epsilon_F \mid + \mid \epsilon_{m'} - \epsilon_m \mid}{2k_B T}\right).$$

where Z_0^{-1} is a prefactor, α^{-1} is the Bohr radius of the localized wave functions, R_m and ϵ_m denote the position and energy of site m. In theory the value of $Z_{mm'}$ is determined by the threshold or critical conductance Z_c, at which the first infinite cluster will form, given by the relation

$$\sigma = \sigma_0 Z_c^{-1}. \tag{44}$$

Here σ_0 is a prefactor. To describe the field-effect mobility in organic transistors, Vissenberg assumed an exponential density of localized states [54].

$$g(\epsilon) = \frac{N_t}{k_B T_0} \exp\left(\frac{\epsilon}{k_b T_0}\right) \qquad (\epsilon \le 0) \tag{45}$$

N_t is the number of states per unit volume and T_0 specifies the width of the exponential distribution. Connecting (1) and (2), conductivity can be described as [54]

$$\sigma(\delta, T) = \sigma_0 \left(\frac{\pi \delta N_t (T_0/T)^3}{(2\alpha)^3 B_c \Gamma(1 - T_0/T) \Gamma(1 + T_0/T)}\right)^{T_0/T}. \tag{46}$$

Here δ is the fraction of occupied states, and B_c is the critical number of bonds per site. Then an expression for

the mobility as a function of the carrier concentration n can be obtained.

$$\mu(n,T) = \frac{\sigma_0}{e}\left(\frac{(T_0/T)^4 \sin(\pi T/T_0)}{(2\alpha)^3 B_c}\right)^{T_0/T} n^{T_0/T-1}. \quad (47)$$

Here e is the elementary charge. However, this expression can not account for the carrier concentration independent mobility when the carrier concentration is very low (LED regime). To overcome this problem, we derive a new mobility model assuming a Gaussian DOS [46] and VRH theory. In this model, the DOS function is given as

$$g(\epsilon) = \frac{N_t}{\sqrt{\pi} k_B T_\sigma} \exp\left[-\left(\frac{\epsilon}{k_B T_\sigma}\right)^2\right]. \quad (48)$$

It is slightly different from [46], where ϵ is the energy measured relative to the center of the DOS and T_σ indicates the width of the DOS. The value of the Fermi energy ϵ_F can be determined by the equation for the carrier concentration n.

$$n = \int_{-\infty}^{\infty} \frac{g(\epsilon)d\epsilon}{1+\exp((\epsilon-\epsilon_F)/k_B T)}. \quad (49)$$

At low n, the exponential function is large compared to one (the nondegenerate case) [56], and we obtain the Fermi energy as

$$\epsilon_F = -\frac{k_B T_\sigma^2}{4T} + k_B T \ln \delta. \quad (50)$$

According to percolation theory [57], at the onset of percolation, the critical number B_c can be written as

$$B_c = \frac{N_b}{N_s}. \quad (51)$$

$B_c = 2.8$ for a three-dimensional amorphous system, N_b and N_s are respectively the density of bonds and density of sites in a percolation system, which can be calculated as [58, 54]

$$N_b = \int d\mathbf{R}_{ij} d\epsilon_i d\epsilon_j g(\epsilon_i) g(\epsilon_j) \theta(s_c - s_{ij})$$

and

$$N_s = \int d\epsilon g(\epsilon) \theta(s_c k_B T - |\epsilon - \epsilon_F|).$$

Here $\mathbf{R_{ij}}$ denotes the distance vector between sites i and j, s_c is the exponent of the conductance given by the relation $\sigma = \sigma_0 e^{-s_c}$ [59] and θ is step function.
Substituting (5) and (7) into (8), we obtain a new percolation criterion for an organic system as

$$B_c \approx \frac{2N_t(\sqrt{2}+1)\sqrt{\pi}}{(2\alpha T/T_\sigma)^3} \cdot \cdot \left(\frac{\epsilon_F + k_B T s_c}{k_B T_\sigma}\right)^2 \exp\left(-\left[\frac{\epsilon_F + k_B T s_c}{k_B T_\sigma}\right]^2\right).$$

This equation has to be solved for s_c and an expression for mobility can be obtained.

$$\mu = \frac{\sigma_0}{eN_t}\exp(\eta) \quad (52)$$

where

$$\eta = -\frac{T_\sigma}{T}\sqrt{-W\left[-\frac{B_c(2\alpha T/T_\sigma)^3}{2\pi N_t(1+\sqrt{2})}\right]} - \frac{T_\sigma^2}{4T^2}$$

W is the Lambert function [60]. Equation (9) is obtained assuming

- that the site positions are random,
- the energy barrier for the critical hop is large,
- and the charge carrier concentration is very low.

Results and Discussions

So far, much attention has been devoted to explain the temperature dependence of the mobility [61, 62]. As shown in Fig. 1, the model (9) gives a non-Arrhenius-type temperature dependence of the form $\mu \propto \exp\left(-(C\sigma/k_B T)^2\right)$, which has also been supported by numerical simulations [63] and analytical calculations [64]. The model (9) shows good agreement for a value $C \approx 0.71$. This value is close to $C \approx 0.69$ given in [65] and 0.64 in [64]. In Fig. 2, the mobility is plotted as a function of $(T_\sigma/T)^{1/3}$. When plotted in this way, there exists the regime with a linear behavior between μ and $T^{-1/3}$. This indicates that variable-range hopping effect has to be taken into account [66, 67].

To obtain (7), a Boltzmann distribution function has been used. The degenerate limit of organic semiconductors has been studied in [68, 69]. In Fig. 3 (a) we show the Fermi energy for Boltzmann and Fermi-Dirac distribution assuming some typical values of the parameter T_σ/T as 1.5, 3.5 and 6.0 [61], Fig. 3 (b) is a comparison especially for the higher carrier occupation regime. The analytical result (7) agrees well with the numerically calculated result for decreasing carrier occupation and increasing T_σ/T. Therefore, for the LED regime with low charge carrier concentration, (7) is a good approximation of the solution of (6).

The mobility as a function of the carrier concentration is presented in Fig. 4, where T_σ/T is in the range $1.5 - 9.0$, corresponding to some typical values for organic semiconductors. The mobility stays constant until a certain threshold value of the carrier occupation. Above this threshold, the mobility can increase about four orders of magnitude at $T_\sigma/T = 9$. These effects

have been observed in the experimental work [53, 70].

However, (9) is valid only in the LED regime with very low carrier concentration. As it is difficult to get an analytical expression for the mobility at higher carrier concentration, we use (4) as the mobility model for the higher carrier concentration. The combined model can explain the experimental data in [70, 53], as shown in Fig. 5.

4.3 Conclusion

An analytical mobility model has been obtained on the basis of variable range hopping theory. This model can explain the relation between mobility and carrier concentration, especially the mobility's independence of the carrier concentration in the LED regime. We can conclude that a Gaussian density of states function is a better description for the low carrier concentration regime than an exponential one. The model also gives non-Arrhenius temperature characteristics.

5 Optimal Design for Carbon Nanotube Transistors

A numerical study of carbon nanotube field effect transistors is presented. To investigate transport phenomena in such devices the non-equilibrium Green's function formalism was employed. Phenomena like tunneling and electron-phonon interactions are rigorously taken into account. The effect of geometrical parameters on the device performance was studied. Our results clearly show that device characteristics can be optimized by appropriately selecting geometrical parameters.

5.1 Introduction

A carbon nanotube (CNT) can be viewed as a rolled-up sheet of graphite with a diameter of a few nano-meters. Depending on the chiral angle the CNT can be either metallic or semiconducting. Semiconducting CNTs can be used as channels for field-effect transistors (FETs). CNTFETs have been studied in recent years as potential alternatives to CMOS devices because of their capability of ballistic transport.

Depending on the work function difference between the metal contact and the CNT, carriers at the metal-CNT interface encounter different barrier heights. Devices with positive [71] and zero [72] barrier heights were fabricated. The barrier height is defined as the potential barrier which is seen by carriers at the Fermi level in the metal. Therefore, in a device with zero barrier height, carriers with energies above the Fermi level of the metal reach the channel by thermionic emission and carriers with energies below the Fermi level have to tunnel to reach the channel. Devices with positive barrier heights have lower on-current and also suffer from ambipolar behavior [73, 74], while devices with zero barrier height theoretically [75] and experimentally [76] show better performance. In this work we focus on devices with zero barrier height for electrons. The barrier height for holes is given by the band gap of the CNT. Since the dispersion relations for electrons and holes are the same, our discussions are valid for holes as well.

Using the non-equilibrium Green's function (NEGF) formalism quantum phenomena like tunneling, and scattering processes can be rigorously modeled. Here we extended our previous work [77] by including the effect of electron-phonon interaction in the calculations, considering large signal dynamic response, and investigating the influence of geometrical parameters. In the next section our methodology is described. Then the effect of different geometrical parameters on the device characteristics is analyzed, and methods for performance optimization are suggested.

5.2 Approach

In this section the models used to study the static and dynamic response of CNTFETs are explained.

5.2.1 Static Response

Based on the NEGF formalism we investigated the effect of device geometry on the performance of carbon nanotube field-effect transistors. We have solved the coupled system of transport and Poisson equations numerically. Due to quantum confinement along the tube circumference, carrier have bound wave functions around the CNT and can propagate along the tube axis. Under the assumption that the potential profile does not vary around the circumference of the CNT, sub-bands will be decoupled. In this work we assume bias conditions for which the first sub-band contributes mostly to the total current. In the mode-space approach [78] the transport equation for each sub-band can be written as:

$$G^{\mathrm{R,A}}_{\mathbf{r},\mathbf{r}'}(E) = [EI - H_{\mathbf{r},\mathbf{r}'}(E) - \Sigma^{\mathrm{R,A}}_{\mathbf{r},\mathbf{r}'}(E)]^{-1} \quad (53)$$

$$G^{<,>}_{\mathbf{r},\mathbf{r}'}(E) = G^{\mathrm{R}}_{\mathbf{r},\mathbf{r}'}(E)\Sigma^{<,>}_{\mathbf{r},\mathbf{r}'}(E)G^{\mathrm{A}}_{\mathbf{r},\mathbf{r}'}(E) \quad (54)$$

In (53) an effective mass Hamiltonian was assumed. All our calculations assume a CNT with a band gap of $\mathrm{E_g} = 0.6\ \mathrm{eV}$ corresponding to a CNT with a diameter of $\mathrm{d_{CNT}} = 1.6\ \mathrm{nm}$, and $m^* = 0.05m_0$ for both electrons and holes. A recursive Green's function method is used for solving (53) and (54) [79]. The total self-energy in (53) consists of the self-energies due to the source contact, drain contact, and electron-phonon interaction, $\Sigma^R = \Sigma^R_{\mathrm{S}} + \Sigma^R_{\mathrm{D}} + \Sigma^R_{\mathrm{el-ph}}$. The self-energy due to electron-phonon interaction consists of the contribution of elastic and inelastic scattering mechanisms, $\Sigma^{<,>}_{\mathrm{e-ph}} = \Sigma^{<,>}_{\mathrm{el}} + \Sigma^{<,>}_{\mathrm{inel}}$. Assuming a single sub-band the electron-phonon self-energies are simplified to (55)-(58).

$$\Sigma^{<,>}_{\mathrm{el},(\mathbf{r},\mathbf{r})}(E) = D_{\mathrm{el}} G^{<,>}_{\mathbf{r},\mathbf{r}}(E) \quad (55)$$

$$\begin{aligned}\Sigma^{<}_{\mathrm{inel},(\mathbf{r},\mathbf{r})}(E) = \sum_\nu & D^\nu_{\mathrm{inel}} \\ & [(n_B(\hbar\omega_\nu)+1)G^{<}_{\mathbf{r},\mathbf{r}}(E+\hbar\omega_\nu) \\ & + n_B(\hbar\omega_\nu)G^{<}_{\mathbf{r},\mathbf{r}}(E-\hbar\omega_\nu)]\end{aligned} \quad (56)$$

$$\begin{aligned}\Sigma^{>}_{\mathrm{inel},(\mathbf{r},\mathbf{r})}(E) = \sum_\nu & D^\nu_{\mathrm{inel}} \\ & [(n_B(\hbar\omega_\nu)+1)G^{>}_{\mathbf{r},\mathbf{r}}(E-\hbar\omega_\nu) \\ & + n_B(\hbar\omega_\nu)G^{>}_{\mathbf{r},\mathbf{r}}(E+\hbar\omega_\nu)]\end{aligned} \quad (57)$$

$$\Im m[\Sigma^{\mathrm{R}}(E)] = \frac{1}{2i}[\Sigma^{>} - \Sigma^{<}] \quad (58)$$

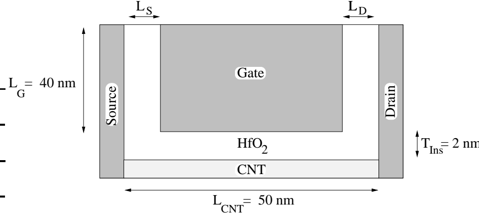

Figure 25: The device structure. The device is 250 nm extended into the third dimension. $\epsilon_r = 15$.

where n_B is given by the Bose-Einstein distribution function. In general electron-phonon interaction parameters ($D_{\mathrm{el,inel}}$) depends on the diameter and the chirality of the CNT. The calculation of these parameters is presented in [80]. The imaginary and real parts of the self-energy broadens and shifts the density of states, respectively. We neglected the real part of the self-energy.

The transport equations (53) to (58) are iterated to achieve convergence of the electron-phonon self-energies, resulting in a self-consistent Born approximation. Then the coupled system of transport and Poisson equation is solved iteratively. The carrier concentration and the current density at some point $\mathbf{r}$ of the device can be calculated as (59) and (60).

$$n_{\mathbf{r}} = -4i \int G^{<}_{\mathbf{r},\mathbf{r}}(E) \frac{dE}{2\pi} \tag{59}$$

$$j_{\mathbf{r}} = \frac{4q}{\hbar} \int \mathrm{Tr}[\Sigma^{<}_{\mathbf{r},\mathbf{r}} G^{>}_{\mathbf{r},\mathbf{r}}(E) - \Sigma^{>}_{\mathbf{r},\mathbf{r}} G^{<}_{\mathbf{r},\mathbf{r}}(E)] \frac{dE}{2\pi} \tag{60}$$

In CNTs elastic scattering is caused by acoustic phonons and inelastic scattering occurs due to zone boundary (ZB), optical (OP), and radial breathing (RBM) phonon modes. In CNTs with diameters in the range $d_{\mathrm{CNT}} = 1-2$ nm, the energies of the these phonon modes are $\hbar\omega_{\mathrm{ZB}} \approx 160$ and 180 meV, $\hbar\omega_{\mathrm{OP}} \approx 200$ meV, and $\hbar\omega_{\mathrm{RBM}} \approx 30$ meV respectively [81, 82]. Due to small occupation number of high energy phonons, such as OP and ZB phonon modes, they do not degrade the performance considerably, whereas the RBM phonon mode can have a detrimental effect. However, due to weak electron-phonon coupling the RBM mode has a negligible effect at room temperature. The electron-phonon coupling is also weak for acoustic phonon (AP) modes. Therefore, short CNTFETs can operate close to the ballistic limit. Figure 26 shows excellent agreement between simulation results and experimental data [76]. The result for the bias point $V_{\mathrm{G}} = -1.3$ V is compared with the ballistic limit, which confirms the validity of nearly ballistic transport in short CNTFETs.

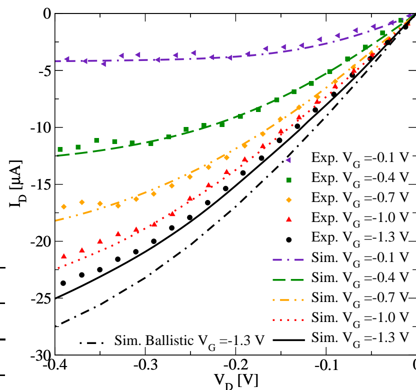

Figure 26: Comparison of the simulation results and experimental data [76] for the output characteristics. The results for the bias point $V_{\mathrm{G}} = -1.3$ V are compared with the ballistic limit.

5.2.2 Dynamic Response

To investigate the dynamic response of the device we consider the device delay time defined as:

$$\tau = \frac{C_{\mathrm{G}} V_{\mathrm{DD}}}{I_{\mathrm{on}}} \tag{61}$$

Here, $C_{\mathrm{G}} = C_{\mathrm{GS}} + C_{\mathrm{GD}} + C_{\mathrm{GG}}$ with ${C_{\mathrm{GG}}}^{-1} = {C_{\mathrm{Ins}}}^{-1} + {C_{\mathrm{Q}}}^{-1}$. The quantum capacitance is given by $C_{\mathrm{Q}} = 8\mathrm{q}^2/\mathrm{h}\nu_{\mathrm{F}} \approx 400\mathrm{aF}/\mu\mathrm{m}$, including the twofold band and spin degeneracy [83, 84]. The insulator capacitance, occurring between the tube and a plane, is given by [85]:

$$C_{\mathrm{Ins}} = \frac{2\pi\kappa\epsilon_0}{\cosh^{-1}(T_{\mathrm{Ins}}/R_{\mathrm{CNT}} + 1)} \tag{62}$$

For the geometry parameters given in Figure 25 $C_{\mathrm{Ins}} \approx 400\mathrm{aF}/\mu\mathrm{m}$. For a device with 50 nm channel length $C_{\mathrm{GG}} \approx 10\mathrm{aF}$. To calculate the gate-source and gate-drain parasitic capacitances we assumed the capacitance of two parallel plates, $C_{\mathrm{GS,GD}} = \kappa\epsilon_0 A/L_{\mathrm{S,D}}$, (see Figure 25). Even with a small total area of $A = 250\ \mathrm{nm} \times 40\ \mathrm{nm}$ and a large spacer width of $L_{\mathrm{GS,GD}} = 10$ nm the parasitic capacitances $C_{\mathrm{GS}} + C_{\mathrm{GD}} \approx 260$ aF are much bigger than C_{GG}. As a result, $C_{\mathrm{G}} \approx C_{\mathrm{GS}} + C_{\mathrm{GD}} = \kappa\epsilon_0 A(1/L_{\mathrm{S}} + 1/L_{\mathrm{D}})$.

5.3 Simulation Results

In this section the effects of the gate-source spacer, gate-drain spacer, insulator thickness, and the insulator dielectric constant on the device characteristics are studied.

Due to ambipolar behavior, in the off-regime the drain current of CNTFETs starts to increase [73, 76, 86]. To reduce this effect we have proposed to increase the gate-drain spacer [77]. When increasing $\mathrm{L_D}$, the off-current decreases, while the on-current remains nearly

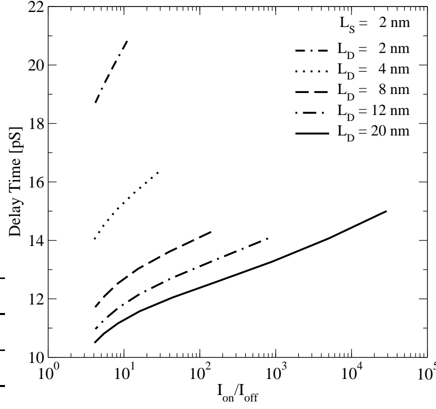

Figure 27: The effect of $L_{\rm D}$ on the device delay time versus $\rm I_{on}/I_{off}$ ratio. $L_{\rm S} = 2\ {\rm nm}$ and $V_{\rm DD} = 0.8$ V.

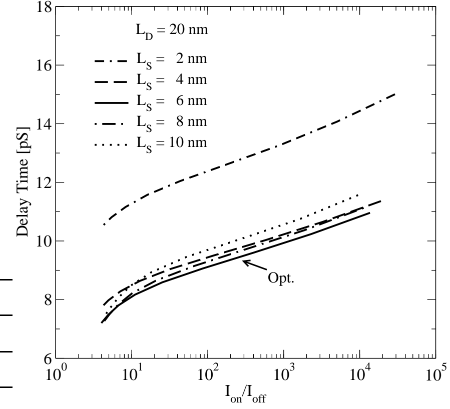

Figure 29: The effect of $L_{\rm S}$ on the device delay time versus $\rm I_{on}/I_{off}$ ratio. $V_{\rm DD} = 0.8\,{\rm V}$. The optimal $L_{\rm S}$ for both device types are shown.

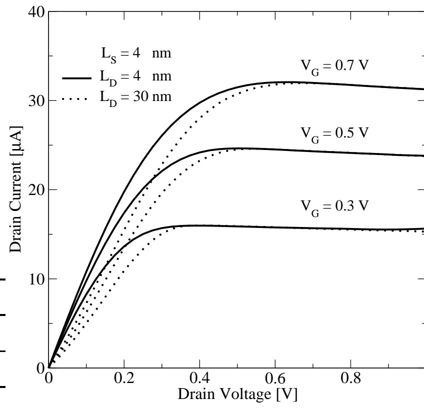

Figure 28: Output characteristics at different gate biases for devices with $L_{\rm D} = 4\,{\rm nm}$ and $L_{\rm D} = 20\,{\rm nm}$. $L_{\rm S} = 4\,{\rm nm}$.

unchanged, such that the $I_{\rm on}/I_{\rm off}$ ratio increases. By increasing $L_{\rm D}$ the gate-drain parasitic capacitance decreases, which results in reducing the device delay time. Figure 27 shows the effect of $L_{\rm D}$ on the device delay time versus $I_{\rm on}/I_{\rm off}$. As shown, a significant performance improvement is achieved. The disadvantage of this method is that at low drain biases electrons have to tunnel through a thicker barrier to reach the drain contact, resulting in a smaller drain current (Figure 28).

When increasing $L_{\rm S}$, the gate-source parasitic capacitance is reduced, and so is the on-current. The band edge profile near the source contact plays an important role in controlling the total current. Increasing $L_{\rm S}$ reduces the gate control of the band-edge profile near the source contact. Both the tunneling current and thermionic emission current contribute to the total current. Electrons with energies lower than the barrier height have to tunnel through the source-sided metal-CNT interface barrier to reach the channel while electrons with energies higher than the barrier height are injected by thermionic emission. Since the tunneling probability decreases exponentially with the barrier width, the tunneling current decreases with increasing $L_{\rm S}$. However, the thermionic emission current is independent of the barrier width. The contribution of the tunneling current decreases with decreasing barrier height, while that of thermionic emission increases. Since τ is proportional to the parasitic capacitance and inversely proportional to the on-current (61), there is an optimal value for $L_{\rm S}$, which minimizes τ. As shown in Figure 29 the optimal value of $L_{\rm S}$ for the given material and geometrical parameters results in optimized device characteristics. It can be easily shown that the optimal value $\rm L_{S0}$, where $\frac{\partial\tau}{\partial L_{\rm S}}|_{\rm L_{S0}} = 0$, is achieved when $\frac{1}{C_{\rm G}}\frac{\partial C_{\rm G}}{\partial L_{\rm S}}|_{\rm L_{S0}} = \frac{1}{I_{\rm on}}\frac{\partial I_{\rm on}}{\partial L_{\rm S}}|_{\rm L_{S0}}$. Considering the expression derived for $C_{\rm G}$ in Section II.B, we have $\frac{1}{C_{\rm G}}\frac{\partial C_{\rm G}}{\partial L_{\rm S}} = [L_{\rm S}(1 + L_{\rm S}/L_{\rm D})]^{-1}$. Figure 30 shows the sensitivity of the on-current to $L_{\rm S}$. However, the mentioned sensitivity is not zero due to the contribution of the tunneling current from states below the Fermi level. Since at positive gate biases the conduction band-edge is pushed below the source Fermi level, even in devices with zero barrier height the tunneling current can contribute to the total current. For thinner insulators the width of the source-sided barrier decreases, resulting in a higher tunneling current contribution to the total current and a higher sensitivity of the on-current to $L_{\rm S}$. The optimal spacer width is $L_{\rm S}\approx$ 6 nm at $T_{\rm Ins} = 2\ {\rm nm}$ and $L_{\rm D} = 20\,{\rm nm}$. Note that the optimal value for $L_{\rm S}$ depends on $L_{\rm D}$. For small values of $L_{\rm D}$ the gate-drain parasitic capacitance dominates the gate-source parasitic capacitance, therefore any further decrease of $L_{\rm S}$ does not improve the delay time.

Electron-phonon interaction reduces the on-current, both, directly and indirectly [87, 88]. The direct effect is due to backscattering of carriers, but scattering also redistributes the carrier concentration profile along the device. This redistribution affects the band-edge profile so that it reduces the total current. To reduce the indirect effect one should increase the gate-CNT

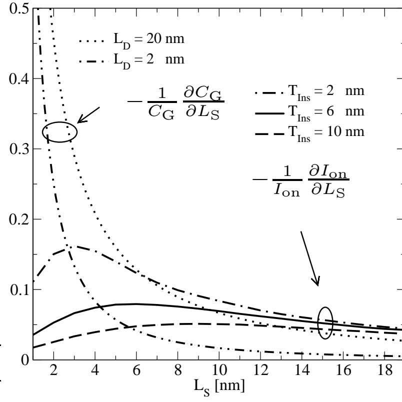

Figure 30: The sensitivity of the parasitic capacitance and the on-current to L_S for different insulator thicknesses. The intersection of the curves gives the optimal L_S, which minimizes τ.

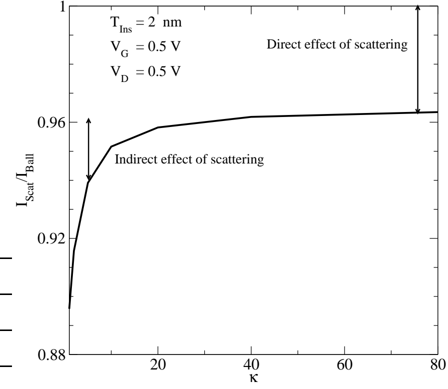

Figure 31: The ratio of the drain current in the presence of scattering to the ballistic limit for different κ. The proportions due to direct and indirect effect of scattering on the on-current are shown. For high-κ the indirect part reduces.

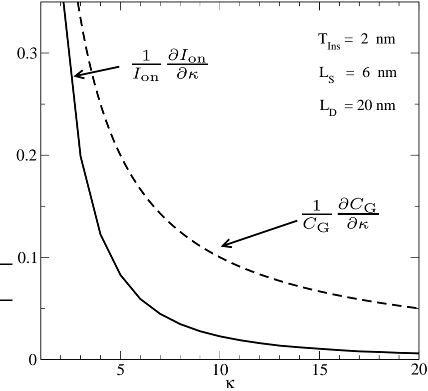

Figure 32: The sensitivity of the parasitic capacitance and the on-current to κ. Since the curves do not intersect at high values of κ lower values of κ minimizes τ.

coupling. If thin and High-κ insulators are used then $C_{\mathrm{Ins}} \gg C_{\mathrm{Q}}$ and $C_{\mathrm{GG}} \approx C_Q$, implying that the potential on the tube becomes the same as the gate (perfect coupling). This regime is called quantum capacitance limit in which the device is potential-controlled rather than charge-controlled [89]. Figure 31 compares the ratio of the current in the presence of scattering to the ballistic limit for different insulators. For the given material and geometrical parameters a $\kappa > 20$ maximizes the performance of the device. But, with using high-κ materials not only the on-current but also the parasitic capacitances increase. Therefore, there is a κ which optimizes the delay time. It can be shown that the optimized value is achieved when $\frac{1}{C_{\mathrm{G}}}\frac{\partial C_{\mathrm{G}}}{\partial \kappa}|_{\kappa_0} = \frac{1}{I_{\mathrm{on}}}\frac{\partial I_{\mathrm{on}}}{\partial \kappa}|_{\kappa_0}$. Considering the expression derived for C_{G} in Section II.B, we have $\frac{1}{C_{\mathrm{G}}}\frac{\partial C_{\mathrm{G}}}{\partial \kappa} = \frac{1}{\kappa}$. Figure 32 shows the sensitivity of the on-current and parasitic capacitances to κ. Since the curves do not intersect at high values of κ, lower values minimizes τ. Therefore, there is a trade-off between device delay time and the on-current. For a specific application this parameter can be optimized.

5.4 Conclusion

We showed that the device characteristics can be optimized by appropriately selecting the geometrical parameters. With increasing the gate-drain spacer, the off-current and the gate-drain parasitic capacitance reduce at the cost of a drain current reduction at low bias voltages. With increasing the gate-source spacer, the drain current and gate-source parasitic capacitance decrease. Since the device delay time is proportional to the parasitic capacitances and inversely proportional to the on-current, there is a value for the gate-source spacer which minimizes the device delay time. The optimal point is where the sensitivity of these quantities are equal. By using high-κ insulators the gate-CNT coupling increases which results in higher on-current, but the parasitic capacitances increase and as a result the device delay time increases.

References

[1] B.W.Sheldon, A.Rajamani, A.Bhandari, S.K.Hong E.Chason, and R.Beresford. Competition Between Tensile and Compressive Stress Mechanisms During Volmer-Weber Growth of Aluminum Nitride Films. *J. Appl. Phy.*, 98:435091–435099, 2005.

[2] R.C.Cammarata, T.M.Trimble, and D.J.Srolovic. Surface Stress Model for Intrinsic Stresses in Thin Films. *J. Mater. Res.*, 15(11), 2000.

[3] M.Platea, W.Brueckner, and H.Wendrock. Stress Evolution During and After Sputter Deposition of Cu Thin Films onto Si (100) Substrates under Various Sputtering Pressures. *J. Appl. Phy.*, 97:549081–549087, 2005.

[4] A. van der Drift. Evolutionary Selection, a Principle Governing Growth Orientation in Vapor-Deposited Layers. *Philips Res. Repts*, 22:267–288, 1967.

[5] Poly-SiGe, a Superb Material for MEMS. In A.Witvrouw, M.Gromova, A.Mechta, S.Sedky, P.DeMoor, and K.Baert, editors, *Proceedings of the MRS Fall Meeting*, 2003.

[6] A.Molfese, A.Mehta, and A.Witvrouw. Determination of Stress Profile and Optimization of Stress Gradient in PECVD Poly-SiGe Films. *Sensors and Actuators A*, 118(2):313–321, 2005.

[7] Ch.Hollauer, H. Ceric, and S. Selberherr. Modeling of Intrinsic Stress Effects in Deposited Thin Films. *Eurosensors 20'th Anniversary*, 1:324–325, 2006.

[8] K. Uchida, R. Zednik, C.H. Lu, H. Jagannathan, J. McVittie, P.C. McIntyre, and Y. Nishi. Experimental Study of Biaxial and Uniaxial Strain Effects on Carrier Mobility in Bulk and Ultrathin-Body SOI MOSFETs. In *IEDM Tech.Dig.*, pp 229–232, 2004.

[9] A. Shimizu et al. Local Mechanical-Stress Control (LMC) : A New Technique for CMOS Performance Enhancement. In *IEDM Tech.Dig.*, pp 433–436, 2001.

[10] J. Welser, J.L. Hoyt, and J.F. Gibbons. NMOS and PMOS Transistors Fabricated in Strained Silicon/Relaxed Silicon-Germanium Structures. In *IEDM Tech.Dig.*, pp 1000–1002, 1992.

[11] K. Rim, J.-L. Hoyt, and J.-F. Gibbons. Transconductance Enhancement in Deep Submicron Strained Si N-MOSFETs. In *IEDM Tech.Dig.*, pp 707–710, 1998.

[12] J.-L. Hoyt et al. Strained Silicon MOSFET Technology. In *IEDM Tech.Dig.*, pp 23–26, 2002.

[13] D. Antoniadis A. Lochfeld. Investigating the relationship between electron mobility and velocity in deeply scaled NMOS via mechanical stress. *IEEE Electron Device Lett.*, 2(12):591–593, 2001.

[14] S. Maikap, C.Y. Yu, S.R. Jan, M.H. Lee, and C.W. Liu. Mechanically Strained Si NMOSFETs. *IEEE Electron Device Lett.*, 25(1):40–42, 2004.

[15] S. Ito et al. Mechanical Stress Effect of Etch-Stop Nitride and its Impact on Deep Submicron Transistor Design. In *IEDM Tech.Dig.*, pp 247–250, 2000.

[16] S. Dhar, H. Kosina, V. Palankovski, E. Ungersboeck, and S. Selberherr. Electron Mobility Model for Strained-Si Devices. *IEEE Trans.Electron Devices*, 52(4):527–533, 2005.

[17] M.M. Rieger and P. Vogl. Electronic-Band Parameters in Strained $\mathrm{Si}_{1-x}\mathrm{Ge}_x$ Alloys on $\mathrm{Si}_{1-y}\mathrm{Ge}_y$ Substrates. *Phys.Rev.B*, 48(19):14276–14287, 1993.

[18] C. Jacoboni and L. Reggiani. The Monte Carlo Method for the Solution of Charge Transport in Semiconductors with Applications to Covalent Materials. *Review of Modern Physics*, 55:645–705, 1983.

[19] C. Jungemann and B. Meinerzhagen. *Hierarchical Device Simulation - The Monte Carlo perspective*. Springer, Wien, New York, 2003.

[20] F.M. Bufler, P. Graf, S. Keith, and B. Meinerzhagen. Full band Monte Carlo Investigation of Electron Transport in Strained Si Grown on $\mathrm{Si}_{1-x}\mathrm{Ge}_x$ Substrates. *Appl.Phys.Lett.*, 70:2144–2146, 1997.

[21] C. Canali, G. Ottaviani, and A. Alberigi-Quaranta. Drift Velocity of Electrons and Holes and Associated Anisotropic Effects in Si. *J.Phys.Chem.Solids*, 32:1707–1720, 1971.

[22] P.M. Smith, M. Inoue, and J. Frey. Electron Velocity in Si and GaAs at Very High Electric Fields. *Appl.Phys.Lett.*, 37:797–798, 1980.

[23] B. Fischer and K. Hofmann. Full band Monte Carlo Model for Electron and Hole Transport in Strained Si Including Inelastic Acoustic Phonon Scattering. *Appl.Phys.Lett.*, 74:2185–2187, 1999.

[24] K. Ismail, S. Nelson, J. Chu, and B. Meyerson. Electron Transport Properties of Si/SiGe Heterostructures: Measurements and Device Applications. *Appl.Phys.Lett.*, 63:660–662, 1993.

[25] W. Hänsch. *The Drift Diffusion Equation and its Application in MOSFET Modeling*. Springer Verlag, Wien, New York, 1991.

[26] I. Balslev. Influence of Uniaxial Stress on the Indirect Absorption Edge in Silicon and Germanium. *Physical Review*, 143:636–647, 1966.

[27] Technische Universität Wien, Austria. *MINIMOS-NT 2.1 User's Guide*, 2004.

[28] S. Dhar, G. Karlowatz, E. Ungersboeck, and H. Kosina. Numerical and Analytical Modeling of the High-Field Electron Mobility in Strained Si. In *Proc. SISPAD*, pp 223–226, 2005.

[29] The MathWorks, Inc. *MATLAB- Language of Technical Computing, User's Guide, Release 14.0*, 2004. http://www.mathworks.com/.

[30] M.V. Fischetti and S.E. Laux. Band structure, deformation potentials, and carrier mobility in strained Si, Ge, and SiGe alloys. *J. Appl. Phys.*, 80(4):2234, 1996.

[31] M.L. Lee, C.W. Leitz, Z. Cheng, A.J. Pitera, T. Langdo, M.T. Currie, G. Taraschi, E.A. Fitzgerald, and D.A. Antoniadis. *Appl. Phys. Lett.*, 79(20):3344, 2001.

[32] A. Ritenour, S. Yu, M.L. Lee, N. Lu, W. Bai, A. Pitera, E.A. Fitzgerald, D.L. Kwong, and D.A. Antoniadis. *IEDM Tech. Dig.*, (433):2003, 2003.

[33] M. Rieger and P. Vogl. Electronic-band parameters in strained Si(1-x)Gex alloys on Si(1-y)Gey substrates. *Phys. Rev. B*, 48(19):14276, 1993.

[34] G. Karlowatz, W. Wessner, and H. Kosina. *Mathmod*, 1:316, 2006.

[35] Institute for Microelectronics TU Wien, http://www.iue.tuwien.ac.at/software/vmc. *VMC 2.0 User's Guide*, 2006.

[36] S. Smirnov, H. Kosina, M. Nedjalkov, and S. Selberherr. *Lecture Notes in Computer Science*, p 185. Springer, 2003.

[37] C. Jacoboni and L. Reggiani. The Monte Carlo method for the solution of charge transport in semiconductors with applications to covalent materials. *Rev. Mod. Phys*, 55(3):645, 1983.

[38] T. Yamada and D.K. Ferry. Monte Carlo Simulation of Hole Transport in Strained Si(1-x)Gex. *Solid State Electron.*, 38(4):881, 1995.

[39] E. Cartier, M.V. Fischetti, E.A. Eklund, and F.R. McFeely. Impact Ionization in Silicon. *Appl. Phys. Lett.*, 62(25):3339, 1993.

[40] S.M. Sze. *Physics of Semiconductor Devices*, p 47. Wiley, New York, 1981.

[41] B. Ghosh, X.F. Fan, and L.F. Register. Monte Carlo Study of Strained Germanium Nanoscale Bulk pMOSFETs. *IEEE Transactions on Electr. Devices*, 53(3):533, 2006.

[42] T. Ghani, M. Armstrong, C. Auth, M. Bost, P. Charvat, T. Hoffmann, K. Johnson, C. Kenyon, J. Klaus, B. McIntyre, K. Mistry, J. Sandford, M. Silberstein, S. Sivakumar, P. Smith, K. Zawadzki, S. Thompson, and M. Bohr. *IEDM Tech. Dig.*, p 978, 2003.

[43] A. B. Walker, A. Kambili, and S. J. Martin. *J. Phys: Condens. Matter*, 14: 9825–9876, 2002.

[44] N. C. Greenham, S. C. Moratti, D. D. C. Bradley, R. H. Friend, and A. B. Holmers. *Nature*, 365:628–630, 1993.

[45] C. J. Drury, C. M. J. Mustaers, C. M. Hart, M. Matters, and D. M. de. Leeuw. *Appl. Phys. Lett*, 73:108, 1998.

[46] H. Bassler. Charge Transport in Disordered Organic Photoconductors. *Phys.Stat.Sol.(b)*, 175:15–56, 1993.

[47] E. Mconwell. *Phys.Rev*, 103(1):51–61, 1956.

[48] N. F. Mott. *J.Phys.*, 34:1356, 1956.

[49] N.F. Mott. *J.Non-Cryst.Solids*, 1:1, 1968.

[50] B. Maennig, M. Pfeiffer, A. Nollau, and K. Leo. *Phys.Rev.B*, 64:1952081–1952089, 2001.

[51] C. Godet. *J.Non-Cryst.Solids*, 299:333–338, 2002.

[52] O. Rubel, S. D. Baranovskii, and P. Thomas. *Phys.Rev.B*, 69:0142061–0412065, 2004.

[53] *Phys.Rev.lett*, 91:216601–216604, 2003.

[54] M. C. J. M. Vissenberg and M. Matters. Theory of the field-effect mobility in amorphous organic transistors. *Phys.Rev.B*, 51:12964–12967, 1998.

[55] A. Miller and E. Abrahams. Impurity conduction at low concentrations. *Phys.Rev*, 120:744–755, 1960.

[56] I. P. Zvyagin and A. V. Plyukhin. *Mos.Univ.Phys.Bull*, 45:84–88, 1990.

[57] V. A. Mbegaokar, B. I. Halperin, and J. S. Langer. Hopping conductivity in disordered systems. *Phys.Rev.B*, 4:2612, 1971.

[58] P. N. Butcher. *Linear and Nonlinear Electron Transport in Solids*. New york, USA: Plenum.

[59] M. Sahimi. *Applications of Percolation Theory*. London, Uk: Taylor Francis, 1994.

[60] R. M. Corless, G. H. Gonner, and D. E. G. Hare. *Adv.Com.Math*, 5:329–359, 1996.

[61] P. M. Borsenberger, E. H. Magin, M. V. der Auweraer, and F. C. de Schryver. *Phys.Status Solidi B*, 175:15, 1993.

[62] C. Godet. *Phil.Mag.Lett*, 83:691–698, 2003.

[63] G. Schonherr, H. Bassler, and M. Silver. *Philos.Mag.B*, 44:369, 1981.

[64] B. Movaghar, M. Grunewald, H. Bassler, and D. Wurtz. *Phys.Rev.B*, 33:5545–5554, 1986.

[65] H. Bassler. Hopping and related phenomena: Advances in disordered semiconductors. *Sigapore: World Scientific*, 1990.

[66] S. Boutiche. http://hal.ccsd.cnrs.fr/docs/00/03/00/ /41/PDF/, 2001.

[67] K. Horiuchi, S. Uchinobu, and A. Hashii. *Appl.Phys.Lett*, 85:1987–1989, 2004.

[68] G. Paasch, P. H. Nguyen, and S. L. Drechsler. *Syn.Metals*, 97:255–265, 1998.

[69] Y. Preezant, Y. Roichman, and N. Tessler. *J.Phys.:Condens.Matter*, 14:9913–9924, 2002.

[70] C. Tanase, P. W. M. Blom, D. M. de Leeuw, and D. Leeuw. *Phys.stat.sol.(a)*, 201:1236–1245, 2004.

[71] J. Appenzeller, M. Radosavljevic, J. Knoch, and P. Avouris. Tunneling Versus Thermionic Emission in One-Dimensional Semiconductors. *Phys.Rev.Lett.*, 92:048301, 2004.

[72] A. Javey, J. Guo, Q. Wang, M. Lundstrom, and H. Dai. Ballistic Carbon Nanotube Field-Effect Transistors. *Letters to Nature*, 424(6949):654–657, 2003.

[73] M. Pourfath, E. Ungersboeck, A. Gehring, B. Cheong, W. Park, H. Kosina, and S. Selberherr. Improving the Ambipolar Behavior of Schottky Barrier Carbon Nanotube Field Effect Transistors. In *ESSDERC*, pp 429–432, 2004.

[74] M. Pourfath, A. Gehring, E. Ungersboeck, H. Kosina, S. Selberherr, B.-H.Cheong, and W. Park. Separated Carrier Injection Control in Carbon Nanotube Field-Effect Transistors. *J.Appl.Phys.*, 97:1,061,031–1,061,033, 2005.

[75] J. Guo, S. Datta, and M. Lundstrom. A Numerical Study of Scaling Issues for Schottky Barrier Carbon Nanotube Transistors. *IEEE Trans. Electron Devices*, 51(2):172–177, 2004.

[76] A. Javey, J. Guo, D. Farmer, Q. Wang, E. Yenilmez, R. Gordon, M. Lundstrom, and H. Dai. Self-Aligned Ballistic Molecular Transistors and Electrically Parallel Nanotube Arrays. *Nano Lett.*, 4(7):1319–1322, 2004.

[77] M. Pourfath, H. Kosina, B. Cheong, W. Park, and S. Selberherr. Improving DC and AC Characteristics of Ohmic Contact Carbon Nanotube Field Effect Transistors. In *ESSDERC*, pp 541–544, 2005.

[78] R. Venugopal, Z. Ren, S. Datta, M. Lundstrom, and D. Jovanovic. Simulating Quantum Transport in Nanoscale Transistors: Real Versus Mode-Space Approaches. *J.Appl.Phys.*, 92(7):3730–3739, 2002.

[79] A. Svizhenko, M. Anantram, T. Govindan, B. Biegel, and R. Venugopal. Two-Dimensional Quantum Mechanical Modeling of Nanotransistors. *J.Appl.Phys.*, 91(4):2343–2354, 2002.

[80] G. Mahan. Electron-Optical Phonon Interaction in Carbon Nanotubes. *Phys.Rev.B*, 68:125409, 2003.

[81] J. Park, S. Rosenblatt, Y. Yaish, V. Sazonova, H. Ustunel, S. Braig, T. Arias, P. Brouwer, and P. McEuen. Electron-Phonon Scattering in Metallic Single-Walled Carbon Nanotubes. *Nano Lett.*, 4(3):517–520, 2004.

[82] R. Saito, G. Dresselhaus, and M. Dresselhaus. *Physical Properties of Carbon Nanotubes*. Imperial College Press, 1998.

[83] P. Burke. AC Performance of Nanoelectronics: Towards a Ballistic THz Nanotube Transistors. *Solid-State Electronics*, 48(10-11):1981–1986, 2004.

[84] D. John, L. Castro, and D. Pulfrey. Quantum Capacitance in Nanoscale Device Modeling. *J.Appl.Phys.*, 96(9):5180–5184, 2004.

[85] P. Burke. An RF Circuit Model for Carbon Nanotubes. *IEEE Trans.Nanotechnology*, 2(1):55–58.

[86] M. Radosavljevic, S. Heinze, J. Tersoff, and P. Avouris. Drain Voltage Scaling in Carbon Nanotube Transistors. *Appl.Phys.Lett.*, 83(12):2435–2437, 2003.

[87] J. Guo and M. Lundstrom. Role of Phonon Scattering in Carbon Nanotube Field-Effect Transistors. *Appl.Phys.Lett.*, 86:193103, 2005.

[88] Guo J. A Quantum-Mechanical Treatment of Phonon Scattering in Carbon Nanotube Transistors. *J.Appl.Phys.*, 98:063519, 2005.

[89] J. Guo, S. Datta, and M. Lundstrom. Assesment of Silicon MOS and Carbon Nanotube FET Performance Limits using a General Theory of Ballistic Transistors. *IEDM Tech.Dig.*, pp 711–714, 2002.